Metamaterial topology optimization of non-pneumatic tires with stress and buckling constraints

Yeshern Maharaj[*]

Kai James[†]

May 2019

Abstract

This paper presents the design of a metamaterial for the shear layer of a non-pneumatic tire using topology optimization, under stress and buckling constraints. These constraints are implemented using global aggregation, for a smooth maximum function. A linear elastic finite element model, implementing solid isotropic material with penalization (SIMP), is used. Design sensitivities are determined by the adjoint method. The method of moving asymptotes (MMA) is used to solve the numerical optimization problem. Two different optimization statements are used. Each requires a compliance limit and some aspect of continuation. The buckling analysis is linear, considering the generalized eigenvalue problem of the conventional and stress stiffness matrices. Various symmetries, base materials and starting geometries are considered. This leads to novel topologies that all achieve the target effective shear modulus of 10 MPa, while staying within the stress constraint. The stress-only designs generally were susceptible to buckling failure. A family of designs (columnar, non-interconnected RUC's) that emerges in this study, appears to exhibit favourable properties for this application.

Keywords: topology optimization, metamaterial design, non-pneumatic tire, stress-constrained optimization, buckling constraints.

Nomenclature

$\boldsymbol{\psi}$ adjoint vector

$\boldsymbol{\rho}$ SIMP, indicator density

$\boldsymbol{k_e}$ element stiffness matrix

$\boldsymbol{K_G}$ global stress stiffness matrix

$\boldsymbol{K}$ global stiffness matrix

[*]Department of Mechanical Engineering, University of Illinois Urbana–Champaign, Urbana, IL, U.S.A., ymahara2@illinois.edu, yeshern@gmail.com

[†]Assistant Professor, Department of Aeronautical Engineering, University of Illinois Urbana–Champaign, Urbana, IL, U.S.A.,kaijames@illinois.edu

$\boldsymbol{R}$	residual vector
$\boldsymbol{u}$	displacement
$\boldsymbol{y}$	state variables in structural analysis
$\boldsymbol{\phi}_j$	j^{th} eigenvector
$\frac{1}{P_j}$	j^{th} eigenvalue
$\overline{\gamma}$	average shear strain
$\overline{\tau}$	average shear stress
$\overline{G}$	effective shear modulus
$\overline{G}^*$	target effective shear modulus
C	compliance
f	function of interest (objective or constraint)
h	shear layer thickness
N_e	number of elements in the RVE (i.e. entire domain)
N_{RUC}	number of representative unit cells in RVE (hence instances of elements with shared densities)
p	SIMP exponent
s_{ij}	global index of element ($j = 1, 2, ... N_{RUC}$) associated with a given ρ_i
ν	Poisson's ratio
$\overline{p}_{contact}$	tire contact pressure
σ	stress

Abbreviations

Cont	multi-limit continuation, optimization statement and associated algorithm
SigTorq	Sigmund & Torquato optimization statement and associated algorithm
DOF	degree of freedom
E-W	east-west (symmetry)
FE	finite element (method, analysis, model)
KKT	Karush-Kuhn-Tucker (conditions)
MMA	method of moving asymptotes
N-S	north-south (symmetry)

NPT   non-pneumatic tire

PEEK polyetheretherketone

RUC   representative unit cell

RVE   representative volume element

SIMP   solid isotropic material with penalization

Superscripts

f free nodes

p prescribed nodes

Subscripts

e (finite) element

li i^{th} linear constraint

lim limit

nli i^{th} nonlinear constraint

VM Von Mises (stress)

1   Introduction
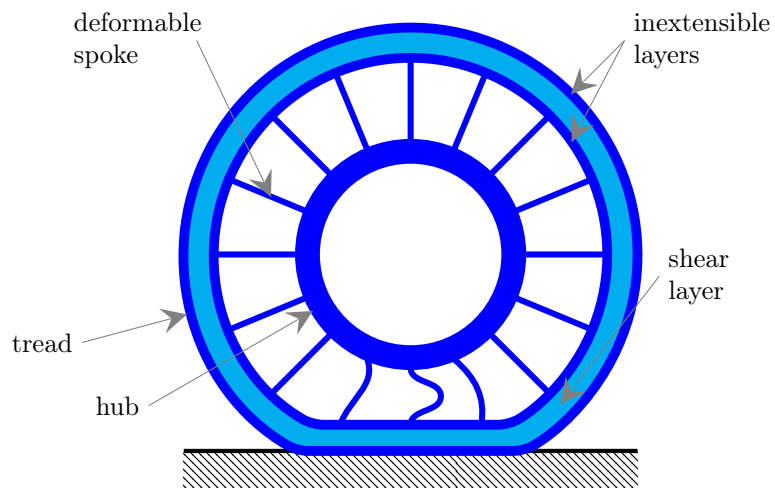
1.1   The non-pneumatic tire

Figure 1: Depiction of a non-pneumatic tire. (Adapted from Czech et al. [1])

The pneumatic tire is so prevalent in modern transport applications that it is often forgotten that the non pneumatic wheel was the state of the art for hundreds of years prior to the invention and adoption of the pneumatic tire. The pneumatic tire has durability and reliability issues in certain applications. The non-pneumatic tire (NPT) is used instead where its inherent robustness is a key design driver. The NPT is less an heir to the solid wheels of past, and more a leap forward in the technology. Rhyne and Cron [2] give an account of the critical characteristics of the pneumatic tire and describe how the technology of the modern NPT can embody these characteristics and surpass them.

The critical characteristics of a pneumatic tire are: low energy loss from obstacle impacts, low mass, low stiffness and low contact pressure [2]. These characteristics are coupled to certain design features in the pneumatic tire. This constrains the design (or application) of pneumatic tires. In the NPT these characteristics can be fulfilled by different features; hence, they can be tailored and optimized further. The NPT has a few main structures: a stiff hub, thin deformable spokes, shear band and tread. Refer to figure 1. The spokes in the region of the ground contact patch deforms (buckles) such that the tension in the opposite side spokes increase to carry the vehicle weight. As per the notation of Rhyne and Cron [2], the NPT is a "top loader" (different from a "bottom loader" e.g. a wagon wheel).

The shear beam of the NPT is a critical feature. It consists of a compliant core with inextensible bands on either side. The nature of this construction and its deformation in the ground contact region implies that the compliant core is nearly in pure shear loading. This shear layer is typically made of an elastomer in order to meet the overall shear beam characteristic. Elastomers (being viscoelastic) have high intrinsic damping as represented by a relatively high loss coefficient. Refer to Ashby [3] for a comparison of the intrinsic damping loss coefficient of various material classes. This leads to a hysteretic energy loss when an elastomer is loaded and unloaded. The hysteretic energy loss increases the material temperature and is dissipated to the environment via heat transfer. This energy loss/inefficiency is registered as part of tire rolling resistance. Given that the other components of rolling resistance (friction and tire aerodynamic losses) are difficult to mitigate, hysteretic losses offer an opportunity for improved fuel economy [4]. The hysteretic loss of the NPT can be reduced by use of a meso-structure or metamaterial composed of material with low intrinsic damping loss coefficient (essentially elastic). See Fazelpour and Summers [5] for an overview of meso-strucutres with respect to the NPT; and Berglind et al. [6], Shankar et al. [7], Czech et al. [1]; for selected specific examples.

1.2   Metamaterial design

By judicious choice of a representative unit cell (RUC) i.e. the smallest repeatable structure, it is possible to tailor a material to have specific beneficial macro-scale properties that are better than those of the constituent material(s). A simple example is a honeycomb for an increased stiffness to mass ratio. Since the seminal paper by Bendsøe and Kikuchi [8], topology optimization has been a technique used in a variety of continuum and structural design investigations [9, 10]. A specific theme is application to material design e.g. materials with extremal elastic properties [11, 12, 13], negative Poisson's ratio [14], optimized thermal expansion [15] and extremal multiphase composites [16]. There are also more established methods of metamaterial design using analytical methods for specific geometries [17]. However, analytical methods have their limitations; for example, deriving the model for complex geometries is difficult [5].

1.3 NPT shear layer metamaterial state of the art

Much of the previous research on NPT metamaterials has been of the analytical/fixed topology type (sizing problem). Shankar et al. [18] presented an analytical model for an auxetic (negative Poisson's ratio) honeycomb mesostructure with sinusoidal re-entrant wall. Kolla et al. [19] implemented a chiral honeycomb structure made of polycarbonate. The model was developed in a commercial finite element (FE) software. Ju and Summers [20] investigated auxetic and conventional honeycombs in aluminium alloy, titanium alloy and high strength steel. Berglind et al. [6] developed a tapered bristle meso-structure in aluminium alloy. Shankar et al. [21] considered an 'S'-type meso-structure, also developed in a commercial FE software. Shankar et al. [7] compared four meso-structures (traditional honeycomb, auxetic, sinusoidal auxetic and S-type). These were optimized using several algorithms - genetic, particle swarm, FAST-SIMPLEX (with response surface). The S-type structure was found to be the most promising.

Thyagaraja et al. [4] created an FE Model of a typical wheel. This was used to determine the shear layer properties required to achieve a maximum shear strain of 10%, similar to an elastomer. That allowed the authors to set the requirements for the metamaterial in order for the NPT to achieve its contact pressure requirements. Czech et al. [22] started a sequence of works that broadly used SIMP topology optimization for the design of the NPT shear layer. This particular paper showed that traditional asymptotic homogenization methods would be inaccurate for an NPT shear layer design, given the difference in length scales. They proposed that an averaging method be used over a representative volume element (RVE).[1]

Homogenization is traditionally used in metamaterial topology optimization [8, 13]. Hassani and Hinton [24] present the theory of homogenization. Drago and Pindera [23] look at RUC and RVE concepts, and the pitfalls of failing to distinguish between them. Broadly, an RVE is made up of a *sufficient* number of RUC's in all dimensions. Only for particular loading and configurations is an RUC also the RVE. Hassani and Hinton [24] emphasize a requirement for homogenization theory to be applicable: *"...in comparison with the dimensions of the body the size of these non-homogeneities should be very small"*. This criterion is not met for a one- or two-RUC deep NPT shear layer metamaterial. Hence, homogenization with periodic boundary conditions over a RUC, is not used in this study.

Czech et al. [25] proposed a "Non-Simply" connected RUC arrangement within the RVE. This model realized a re-entrant auxetic honeycomb topology. Czech et al. [1] used the globally optimized results from Thyagaraja et al. [4] as input to the metamaterial topology optimization of the shear layer. This was performed mainly using polycarbonate as a candidate material for a range of optimal shear layer thicknesses and metamaterial shear modulus combinations. It returns the auxetic honeycomb for certain runs, and returns various cross or diamond configurations for others. This work did not consider stress nor buckling constraints. Czech [26] provides further discussion on optimization including design sensitivities and choice of optimization problem statement.

This paper extends the topology optimization work for the NPT shear layer by including stress and buckling constraints. This design optimization is achieved through the introduction of two distinct optimization problem formulations, along with the use of a novel windowing strategy. By applying windowing to the RVE, we negate end effects on the computational domain, improving modeling efficiency. We investigate the impact of various symmetries and starting configurations. We only consider the canonical case of average shear strain, $\overline{\gamma} = 10\%$ and effective shear modulus, $\overline{G} = 10$ MPa. This corresponds to a shear layer thickness of 7 mm (Thyagaraja et al. [4], for both orthotropic and isotropic material cases).

---

[1]The smallest volume that *"characterizes statistically heterogeneous materials at an appropriate scale"* - Drago and Pindera [23].

The rest of the paper is organized as follows: Section 2 provides the problem description and the optimization problem statement. Section 3 presents the sensitivity analysis approach; and the stress and buckling constraints. Section 4 details aspects of the implementation, including the choice of RVE used in the optimization, and methods to increase discretization while remaining computationally tractable. In section 5 we outline the choice of base materials used in the study. Section 6 shows the results using the stress constraint, and the results using both the buckling and stress constraints. In Section 7 we summarize the results and draw conclusions.

2 Problem description
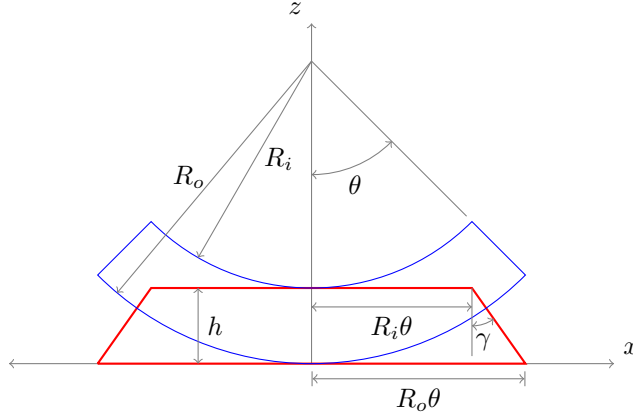
Figure 2: Idealized contact section of the NPT, deformed in red, undeformed in blue. (Adapted from Rhyne and Cron [2])

Assuming $h \ll R$ and using the idealized geometry of the contact region (figure 2), the result is that the shear strain varies linearly with the distance from the centre of the contact region: $\gamma = \arctan(x/R)$. Hence, the shear strain is at its maximum at the edge of the contact region - the most onerous deformation seen by the prospective metamaterial. By considering a vertical force balance, we arrive at the following relation for (average) contact pressure, $\bar{p}_{contact}$, in terms of the effective shear modulus, $\overline{G}$, tire radius, R, and shear layer thickness, h, [2]:

$$\bar{p}_{contact} \approx \frac{\overline{G}h}{R}.$$ (1)

While equation 1 is true on average, the local contact pressure varies with distance from the centre of the region as well, peaking in the middle and vanishing at the ends [4].
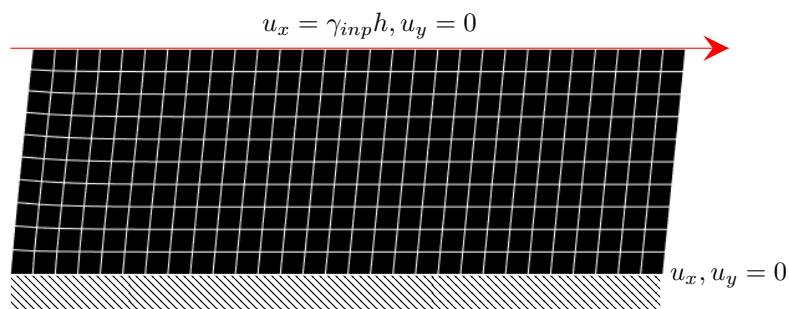
2.1 Structural model

$$u_x = \gamma_{inp}h, u_y = 0$$

$$u_x, u_y = 0$$

Figure 3: Domain of FE Model (discretization not to scale) and loading

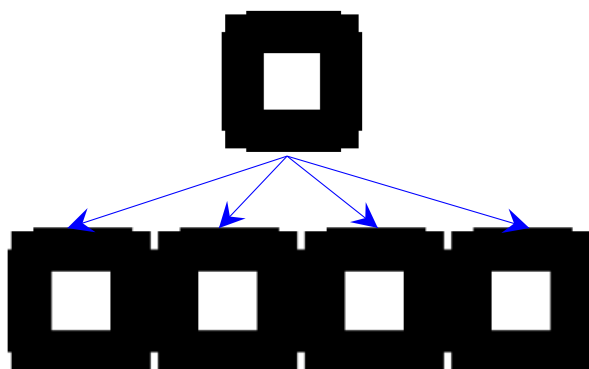**Figure 4:** The RUC is a repetitive structure within the RVE

Table 1: Model parameter values

Parameter	Value[2]
Shear layer thickness, h [mm]	7
Tire mean radius, R [mm]	240
Effective shear modulus, $\overline{G}$ [MPa]	10
Shear strain, $\overline{\gamma}$	0.1
Tire thickness [mm]	200
RVE width	$2h$
Discretization of RUC	128x128

We create a finite element model with 2-D, 4 node isoparametric elements, assuming plane stress conditions. The elements cover a rectangular domain (figure 3) of the prospective shear

---

[2]Values informed by [4], except for RVE size and discretization - refer to section 4.5.

7

layer RVE in preparation for a (material design) *layout optimization* [9]. Notwithstanding the complexities of even the idealized NPT deformation and loading described above, we apply a fixed horizontal load on the top boundary of the domain [1]. We will optimize with a domain $2h$ wide (further explanation is given in section 4.5). The region of peak shear strain is not the entire contact patch. We assume material and geometric linearity. This assumption is justified by the fact that we constrain stresses to be below the yield threshold of the chosen materials. Furthermore, we apply displacement-controlled loads, which lead to small strains that enable the use of a linear elastic model. The traditional form of the SIMP model is applied [27]:

$$E = \tilde{\rho}^p E_0, \tag{2}$$

where E_0 is the Young's Modulus of the base material, $p > 1$ is the SIMP penalization exponent, $\tilde{\rho}$ is the filtered indicator density and E is the effective Young's modulus of the local material. This formulation penalizes intermediate densities to force a discrete $(0, 1)$ design, while allowing for continuity. We typically take $p = 4$, [28, 26].

2.2   Optimization problem statement

The average strain is defined as follows:

$$\overline{\gamma} = \frac{1}{V_{RVE}} \int_{\Omega_0} \gamma d\Omega_0. \tag{3}$$

It is included for completeness. The fixed input displacement, implies an average strain (the selected 10%). Hence this definition is not required for the loading used. The average shear stress, $\overline{\tau}$, is:

$$\overline{\tau} = \frac{1}{V_{RVE}} \int_{\Omega_0} \tau d\Omega_0, \tag{4}$$

where Ω_0 is the RVE domain and V_{RVE} is the (dimensional) volume of the RVE. The average shear modulus is then:

$$\overline{G} = \frac{\overline{\tau}}{\overline{\gamma}}. \tag{5}$$

Recall from equation 1 that the average contact pressure is proportional to $\overline{G}$. A lower $\overline{G}$ (i.e. lower than can be provided by monolithic low-loss materials) stems from limitations on allowable tire contact pressure, which in turn stem from higher level requirements like passenger comfort and high speed dynamic loading [1]. The compliance, C, is defined as:

$$C = \boldsymbol{F}^p \cdot \boldsymbol{u}^p. \tag{6}$$

The design variables are the indicator densities ρ_i of the RUC (noting that several elements, one in each RUC, will share a ρ_i to enforce periodicity across the RUC's.)

8

Two optimization problem statements are considered:

$$
\begin{aligned}
\text{Minimize:} \quad & \overline{G} \\
\text{w.r.t} \quad & \rho_i \\
\text{s.t.} \quad & \\
g_{l1} \quad = \quad & V - V_{lim} \leq 0, \\
g_{l2} \quad = \quad & 0 \leq \rho_{min} \leq \rho_i \leq 1, \\
g_{nl1} \quad = \quad & C_{lim} - \boldsymbol{F}^p \cdot \boldsymbol{u}^p \leq 0, \\
g_{nl2} \quad = \quad & \left[\sum_{i=1}^{N_e} \left(\rho_i{}^\eta \frac{\overline{\sigma}_{VM,i}}{\sigma_{lim}} \right)^q \right]^{\frac{1}{q}} - (1 + \epsilon) \leq 0, \\
g_{nl3} \quad = \quad & \left[\sum_{j=1}^{N_{eig}} \left(\frac{P_{lim}}{P_j} \right)^q \right]^{\frac{1}{q}} - (1 + \epsilon) \leq 0,
\end{aligned}
\tag{7}
$$

and:

$$
\begin{aligned}
\text{minimize:} \quad & V + Error_G \\
\text{w.r.t} \quad & \rho_i \\
\text{s.t.} \quad & \\
g_{l2} \quad = \quad & 0 \leq \rho_{min} \leq \rho_i \leq 1, \\
g_{nl1} \quad = \quad & C_{lim} - \boldsymbol{F}^p \cdot \boldsymbol{u}^p \leq 0, \\
g_{nl2} \quad = \quad & \left[\sum_{i=1}^{N_e} \left(\rho_i{}^\eta \frac{\overline{\sigma}_{VM,i}}{\sigma_{lim}} \right)^q \right]^{\frac{1}{q}} - (1 + \epsilon) \leq 0, \\
g_{nl3} \quad = \quad & \left[\sum_{j=1}^{N_{eig}} \left(\frac{P_{lim}}{P_j} \right)^q \right]^{\frac{1}{q}} - (1 + \epsilon) \leq 0,
\end{aligned}
\tag{8}
$$

where $V = \frac{1}{N_{e,RUC}} \sum_{i=1}^{N_e} \rho_i$, is the normalized volume and $N_{e,RUC}$ is the number of elements in the RUC for the volume constraint. The term $Error_G$ is the error in achieving the required effective shear modulus. It is scaled to be similar in magnitude to the normalized volume so that it does not dominate the objective function during the optimization routine. It is defined as follows:

$$
Error_G = \frac{\left(\overline{G} - \overline{G}^* \right)^2}{\left(\overline{G} + \overline{G}^* \right)^2}.
\tag{9}
$$

Furthermore, this error term has the beneficial properties of always being positive and smooth throughout the design domain. The non-linear constraints on stress and buckling (g_{nl2} and g_{nl3}) are explained in section 3. Note that we have applied a lower bound on the compliance due to the fact that the finite element analysis uses displacement control as opposed to force control. This constraint ensures that a nominal stiffness is achieved. It is required for both statements, but especially so for the first, where without it, the optimization would return a trivial solution - all elements at $\rho = 0$. Note also that while some authors have achieved target material properties through the use of an explicit constraint of the form $\overline{G} - \overline{G}^* = 0$, Bendsøe and Sigmund [10] argues against this form of targeted constraint on the grounds that not all target material properties can be achieved for given inputs.

Notwithstanding the power of optimization with design sensitivities and mathematical programming techniques, both statements address a fundamental issue in material design: initial guesses (starting geometries) are typically far from the constraint boundaries, hence infeasible. As shall be seen in the implementation (in section 4), the first statement is computationally robust. By including the compliance constraint, we prevent the trivial solution. We minimize

$\overline{G}$ for a given volume i.e. we do not ask the optimizer for a particular value, but the minimum for a given volume, hence improve the statistical probability of achieving the required $\overline{G}$ by progressively lowering the volume limit. A continuation method is applied for the various limits to achieve the target shear modulus in a manner consistent with other studies [29, 30]. The second statement is informed by Sigmund and Torquato [15] , hence is also with precedence.. The composite cost function is pseudo-Langrangian in form. The advantage of this statement is that a priori knowledge of the highest likelihood V that will meet the requirements, is unnecessary.

3 Sensitivity analysis, stress and buckling constraints

Given the large number of design variables, the sensitivities are calculated analytically by adjoint method (rather than via computationally costly finite differences) - refer to Sobieszczanski-Sobieski [31] for the base theory; and James and Waisman [32] for a detailed example. The sensitivity of the objective function in FE form follows:

$$\frac{d\overline{G}}{d\rho_i} = p\rho_i{}^{p-1} \sum_{j=1}^{N_{RUC}} \left(\frac{G_0}{N_e \overline{\gamma}_{inp}} \boldsymbol{\beta}_{row3} + \boldsymbol{\psi}_{e,s_{ij}}{}^T \boldsymbol{k_{e0}} \right) \cdot \boldsymbol{u}_{e,s_{ij}}, \qquad (10)$$

where N_e is the number of elements in the RVE (i.e. entire domain), N_{RUC}, is the number of representative unit cells in RVE (hence instances of elements with shared densities), G_0 is the base material shear modulus, $\overline{\gamma}_{inp}$ is the shear strain associated with the loading, $\boldsymbol{\beta}$ is a Gauss integrated matrix (refer to equation 30), $\boldsymbol{\psi}_{e,s_{ij}}$ is the element adjoint term relevant to this function (refer to equation 29), $\boldsymbol{k_{e0}}$ is the element stiffness (without the SIMP term) and $\boldsymbol{u}_{e,s_{ij}}$ is the element displacement. Refer to Appendix B for the derivation. The compliance function sensitivity is given by:

$$\frac{dg_{nl1}}{d\rho_i} = -\frac{dC}{d\rho_i} = - \sum_{j=1}^{N_{RUC}} \boldsymbol{u}_{e,s_{ij}}{}^T p\rho_i{}^{p-1} \boldsymbol{k_{e0}} \boldsymbol{u}_{e,s_{ij}}, \qquad (11)$$

where C is the compliance - refer to equation 6.

To prevent "checkerboarding" and mesh dependency [33], a density filter[3] is applied. The filter sets the length scale of features within the structure. We refer the reader to Bruns and Tortorelli [35] for the detail of a typical implementation. In the results presented later we apply a filter radius of twice the element width, unless otherwise noted.

3.1 Stress constraints

Stress constraints have been extensively investigated in the topology optimization context. Cheng and Guo [36] presented an ϵ-relaxed formulation for trusses under stress constraints. Duysinx and Bendsøe [37] applied stress constraints to topology optimization problems for composites and SIMP. They included relaxation of the constraint for low density elements to prevent degeneracy or singularity. Degeneracy occurs due to the discontinuous nature of the stress constraint when the truss cross-section or element density tends to zero, causing convergence to local optima. They applied the stress constraint locally (i.e. per element). James et al. [38] explained that this can lead to a prohibitively large number of constraints. However, they circumvent this by only considering a subset of active constraints in their algorithm.

---

[3] *"...blurring techniques borrowed from image processing"* - Sigmund [34]

An alternative is to aggregate the stress constraints - *global aggregation* [39]. They consider two forms for the global function - Kreisselmeier-Steinhauser and a *q-norm* function that is effectively a smooth maximum function. Paris et al. [40] consider an intermediate version, *block aggregation*, where the aggregation is applied over groups of elements rather than the entire domain. This method was used in Lee et al. [30] to investigate design-dependent loading. Le et al. [41] present an extensive review of the stress constraint functions, their implementation and parameters. They further modify the regional stress measure (*interlacing*) to group elements that are not necessarily connected.

In this study we apply a single *q-norm* aggregation to the element average Von Mises stress, over the entire RVE:

$$g_{nl2} = \left[\sum_{i=1}^{N_e} \left(\rho_i{}^\eta \frac{\overline{\sigma}_{VM,i}}{\sigma_{lim}} \right)^q \right]^{\frac{1}{q}} - (1 + \epsilon) \leq 0, \tag{12}$$

where $\overline{\sigma}_{VM,i}$, is the element average Von Mises stress, σ_{lim}, is an applicable material stress limit and ϵ, is a small number (1×10^{-6}). We select the stress relaxation exponent, $\eta = 1$, and the aggregation exponent, $q = 10$. The sensitivity in FE form is:

$$
\begin{aligned}
\frac{dg_{nl2}}{d\rho_i} = (\eta + p)\, \rho_i{}^{[(\eta+p)q-1]} \Upsilon^{\frac{1-q}{q}} \sum_{j=1}^{N_{RUC}} \left(\frac{\Delta_{s_{ij}}{}^{\frac{1}{2}}}{\sigma_{lim}} \right)^q \\
+ p\rho_i{}^{p-1} \sum_{j=1}^{N_{RUC}} \boldsymbol{\psi}_{e,s_{ij}}{}^T \boldsymbol{k_{e0}} \cdot \boldsymbol{u}_{e,s_{ij}},
\end{aligned}
\tag{13}
$$

where $\Delta_{s_{ij}}$, is a function of element displacements (equation 37), Υ is a grouping of terms (equation 39) and $\boldsymbol{\psi}_{e,s_{ij}}$ is the element adjoint vector relevant to this function (equations 29 and 40). The derivation is found in Appendix C.

3.2 Buckling

Buckling as a failure mode has also been investigated in previous topology optimization studies. Papers by Neves et al. [42] and Rodrigues et al. [43], are foundational on the topic. Neves et al. [42] argues the need for buckling analysis, as topology optimization in low volume fraction designs inevitably leads to slender structures that can be prone to this failure mode. They considered the eigenvalues of a linear structural model. Given the number of eigenvalues, the problem is a non-smooth optimization and they approached this with the concept of a generalized gradient [44]. Neves et al. [45] extended this work to local buckling with homogenization in periodic materials. Pedersen [46] considered eigenvalues in the topology optimization of an Atomic Force Microscope.

Gao and Ma [47] investigated various aspects of topology optimization with buckling constraints. Their numerical example was a column under a distributed load with volume constraint. Compliance was minimized. An assumed stress element was used in the finite element formulation [48]. An energy based method was proposed for exclusion of pseudo (artificial) modes. They also tested various continuation algorithms (i.e. solve the compliance minimization problem under a volume constraint, then use that geometry as the starting point for the buckling problem.)

Given the low volume fractions of the NPT shear layer, we consider that buckling is a case to investigate. We will approach buckling in a manner similar to the stress constraint i.e. use a *q-norm* function. Aggregation for buckling constraints was tested with success in Ferrari and Sigmund [49]. They tested an incompatible element (Q6) as well as the traditional 4-node

isoparametric element. Though the incompatible element was theoretically superior, the performance of 4-node quads even for slender structures within continuum domains, was comparable to the incompatible elements. As per their study, we will consider the linear buckling case. The constraint function is given by:

$$g_{nl3} = \left[\sum_{j=1}^{N_{eig}} \left(\frac{P_{lim}}{P_j} \right)^q \right]^{\frac{1}{q}} - (1 + \epsilon) \leq 0, \tag{14}$$

where N_{eig} is the number of largest eigenvalues monitored (12 used in study) and P_{lim} is a multiplier for the margin to the eigenvalue. The quantity, $\frac{1}{P_j}$, is an eigenvalue of the generalized problem of the geometric (stress) stiffness ($\boldsymbol{K_G}$) and conventional stiffness matrices.:

$$\left(\boldsymbol{K_G}^{\boldsymbol{ff}} + \frac{1}{P_j} \boldsymbol{K^{ff}} \right) \boldsymbol{\phi}_j = \boldsymbol{0}. \tag{15}$$

Here $\boldsymbol{\phi}_j$ is the eigenvector associated with $\frac{1}{P_j}$, and:

$$\frac{1}{P_j} = - \frac{\boldsymbol{\phi}_j^T \boldsymbol{K_G}^{\boldsymbol{ff}} \boldsymbol{\phi}_j}{\boldsymbol{\phi}_j^T \boldsymbol{K^{ff}} \boldsymbol{\phi}_j}. \tag{16}$$

The element stress stiffness is defined in equation 42.

It is known that artificial modes appear in low density elements [42, 45, 10]. Neves et al. [45] used a cutoff, $\rho_i < 0.1$ to exclude these elements from the stress stiffness matrix. We will implement this approach.

Further, Bendsøe and Sigmund [10] suggest an alternate penalization for stress vs conventional stiffness matrices:

$$\begin{aligned} \text{For } \boldsymbol{K}: \quad E &= \left[\rho_{min} + (1 - \rho_{min}) \rho^p \right] E_0, \\ \text{For } \boldsymbol{K_G}: \quad E &= \rho^p E_0. \end{aligned} \tag{17}$$

Ferrari and Sigmund [49] implemented this with success (though they did go lower than the traditional $\rho_{min} = 0.001$ value), however, for this study, equation 17 led to non-contiguous topologies, hence we propose the following:

$$\begin{aligned} \text{For } \boldsymbol{K}: \quad E &= \rho^p E_0, \\ \text{For } \boldsymbol{K_G}: \quad E &= \rho^{p+1} E_0. \end{aligned} \tag{18}$$

For $\rho \approx 1$, equation 18, has little impact. As $\rho \to 0$, the geometric stiffness matrix is penalized heavily. By using the slightly higher SIMP exponent for the stress stiffness matrix ($p + 1$), we can keep $\rho_{min} = 0.001$ to be consistent with our stress-constraint-only optimizations, and still achieve contiguous buckling designs. Our dual focus on stress- and buckling-constrained designs necessitates a careful balance between the penalization exponent and the minimum density limit (ρ_{min}). The sensitivity of the buckling constraint is as follows:

$$\begin{aligned} \frac{dg_{nl3}}{d\rho_i} = & p\rho_i^{p-1} \sum_{m=1}^{N_{RUC}} \boldsymbol{\psi}_{e,s_{im}}^T \boldsymbol{k_{e0}} \cdot \boldsymbol{u}_{e,s_{im}} \\ & + P_{lim} \Upsilon_b^{\frac{1-q}{q}} \sum_{m=1}^{N_{RUC}} \sum_{j=1}^{N_{eig}} \left(\frac{1}{P_j} \right)^{q-1} \frac{1}{\Theta_{K,j}^2} \times \\ & \left((p+1)\rho_i^p \Theta_{K,j} \left(\boldsymbol{\phi}_{e,j}^T \boldsymbol{\kappa \kappa_{Ge0}} \boldsymbol{k_{uGe,s_{im}}} \boldsymbol{\phi}_{e,j} \right) + p\rho_i^{p-1} \Theta_{G,j} \left(\boldsymbol{\phi}_{e,j}^T \boldsymbol{k_{e,0}} \boldsymbol{\phi}_{e,j} \right) \right), \end{aligned} \tag{19}$$

where Υ_b is a grouping of terms (equation 50) and $\boldsymbol{\psi}_{e,s_{i_j}}$ is the element adjoint vector relevant to this function (equations 29 and 51), $\Theta_{G,j}$ and $\Theta_{K,j}$, are terms related to the numerator and denominator of the eigenvalue j, respectively, (equation 50). Stress stiffness related matrices, $\boldsymbol{\kappa\kappa_{Ge0}}$ and $\boldsymbol{k_{uGe,s_{im}}}$ are defined in equation 47. The detailed derivation is found in Appendix D.

4 Implementation

The finite element model and associated optimization is implemented in Matlab. In-built functions for the Cholesky decomposition and sparse matrix handling, are used for improved numerical efficiency. The eigenvalues are determined using the Matlab function, "eigs". As is good practice for such involved functions for sensitivity, their implementation is verified by a finite difference calculation. Note that $\rho \in [0.001, 1]$. The minimum density, ρ_{min}, is chosen at a typical value for a linear analysis to avoid numerical instabilities. The MMA algorithm from Svanberg [50, 51], allows for efficient optimization. It creates analytical convex approximations of the non-linear functions. The Matlab MMA implementation (courtesy of Krister Svanberg) is used.

4.1 The Continuation method

For the first problem statement, we apply a continuation method as the backbone of the optimization. James et al. [29] used continuation for optimization of the stiffness of structures under multiple load cases. The SIMP exponent and aggregation parameter were varied as part of the algorithm, in that study. Lee et al. [30] also used continuation in a design-dependent optimization. There, the two-stage continuation also included switching from compliance minimization to weight minimization under stress constraints. Continuation methods have been applied to several different topology optimization parameters, for example the filter radius in Sigmund [52]. Gao and Ma [47] used continuation in a buckling optimization.
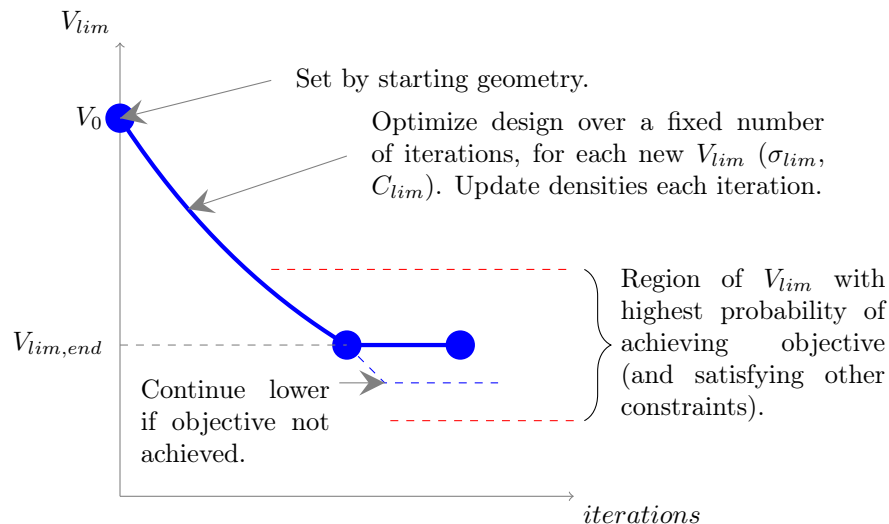
Figure 5: The volume limit as a function of iterations, illustrating continuation method.

Table 2: The optimization algorithm with continuation

No.	Pseudo code	Note
1:	$V^{(0)}, C^{(0)}, \sigma_{VM,max}{}^{(0)}, \overline{G}^{(0)} \leftarrow$ FE model	▷ For some starting structure, solve forward problem. Superscript (0) indicates the values computed based on the starting geometry.
2:	$k_{max} \leftarrow 100$, $k_e \leftarrow 50$,	▷ Maximum iterations and iteration for end of continuation.
3:	$V_{lim}^{(e)}, C_{lim}^{(e)}, \sigma_{lim}^{(e)}$	▷ Based on numerical testing and material requirements select end limits. Note that superscript (e) indicates the terminal values of the constraint limits enforced at the end of the continuation phase.
4:	for $k \leftarrow 1, 2, ...k_{max}$ do:	▷ Start optimization loop.
5:	if $k \leq k_e$ e.g. $V_{lim}^{(k)} \leftarrow V^{(0)} \left(\frac{V_{lim}^{(e)}}{V^{(0)}} \right)^{\frac{k-1}{k_e-1}}$	▷ Change limits. Note that superscript (k) indicates the values values computed at the current iteration k.
6:	if $k > k_e$ and $k < k_{max}$ e.g. $V_{lim}^{(k)} \leftarrow V_{lim}^{(e)}$	▷ Outside of continuation phase, limits are constant.
7:	$\boldsymbol{u^{(k)}}, \frac{d\overline{G}}{d\rho_i}{}^{(k)}, \frac{dg_{nl2}}{d\rho_i}{}^{(k)}$, etc. $\leftarrow$ FE model	▷ Solve forward problem at current limits and calculate sensitivities (required to create MMA convex approximations).
8:	e.g. Min. $f = \overline{G}$ $\boldsymbol{\rho^{(k)}} \leftarrow$ MMA	▷ Minimise objective with constraints using MMA and update densities. One can optimize at intermediate limits (within an interior loop) until the kktnorm is below its limit, however this increases overall solution time without significantly altering or improving the final topology. Hence we recommend one MMA iteration per intermediate limit and a large k_e (i.e. small change in limits per loop increment).
9:	exit loop if $k > k_{max}$ or $kktnorm < kktnorm_{lim}$ & $k > k_e$	▷ Terminate the optimization loop if kktnorm is below limits and we are outside of continuation phase or we have reached maximum iterations.
10:	if $\overline{G} > \overline{G}^* + \epsilon$ go to step 2, lower $V_{lim}^{(e)}$ or $C_{lim}^{(e)}$	▷ Return to step 2 if the effective shear modulus is above that required. Start with the geometry of the k_{max} step and lower the limits. Reset k.

Our method is described in table 2 and figure 5. The stress limit at the end, $\sigma_{lim,end}$, is simply the required fatigue stress limit for the base material. The end limits, $V_{lim,end}$ and $C_{lim,end}$, were selected based on values most likely to achieve the objective and satisfy the constraints. These values constituted a design choice that was informed by numerical experiments. As will be seen,

there is an inverse relationship between the base material elastic properties and the $V_{lim,end}$ most likely to give the required objective and satisfy the constraints. A geometric increment was used for the varying limit phase (i.e. the limits are reduced by a constant fraction per increment). A linear decrement method was also tried, as were lower k_e, e.g. $k_e = 20$. Topologies achieved were broadly similar; however, the approach described in step 8 of table 2 was eventually chosen, based on numerical results.

We take an MMA kktnorm limit of 0.001 in order to terminate the optimization. However, there were instances in which the kktnorm stagnated at higher values.

The continuation method described in table 2 is traditionally implemented to increment the SIMP exponent in compliance minimization problems from one to the final value, principally to circumvent local minima [53]. However, in this case, including the SIMP exponent in our continuation algorithm did not improve the results, hence we kept this value constant.

For the Sigmund & Torquato composite objective, continuation on the volume limit is unnecessary. We also keep the compliance limit constant (the value informed from our first problem statement analysis runs - typically a per volume compliance value $\approx 2 \times 10^5 J/m^3$, was used). The stress limit is incremented as per the above described algorithm.

A compliance constraint is a floor of both algorithms optimization routines. The form of the sensitivity of the compliance function is the same as that for mutual energy when applying the unit strain load case(s), during typical metamaterial design [11, 13]. (Non-dimensional or unit elastic properties are usually also applied i.e. $E_0 = 1$, for traditional metamaterial design.) Hence, there is a close relationship between the compliance and the effective shear modulus [1]. If the starting structure is uniform (say all elements at $\rho = 0.6$) that the optimizer will not create a "SIMP convergent" design i.e. it will tend to a design with all densities at similar values - not black and white [26]. Hence, black and white starting structures must be chosen. Czech et al. [1] tried four starting structures, predominantly solid, with a single notch or four small notches. We will investigate these and other starting structures, including randomly generated ones. We will generally set the shear layer to be 1 RUC thick. Czech et al. [1] did not achieve required shear modulus with 2 or more layers, except for the nonsimply connected implementation.
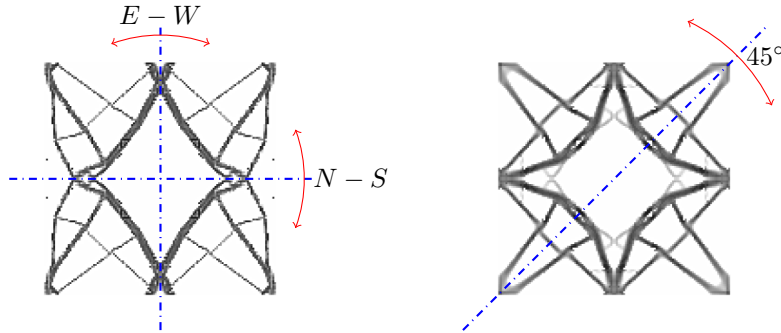
4.2 Symmetries

Figure 6: N-S, E-W and additional 45° symmetry

We consider a North-South, (N-S) and East-West (E-W) symmetry (figure 6). Given the idealized deformation of the NPT shear layer (see figure 2), invariance in performance and other figures of merit are required in the East-West direction. An additional 45° symmetry is also considered in certain instances for sake of exploring different geometries.
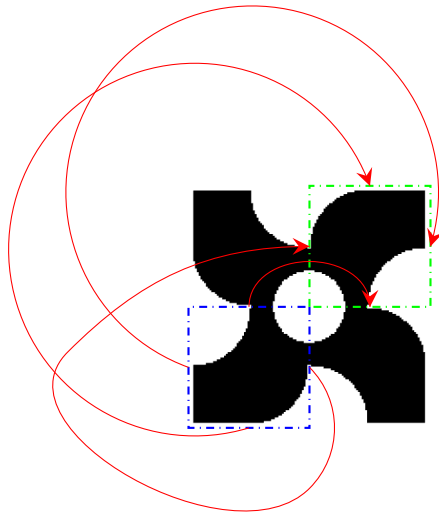
15

Figure 7: 4-fold rotational symmetry.

In the same vein, we consider a rotational symmetry - figure 7. Here, the E-W invariance of the design is to be confirmed by loading in the opposite direction (or testing E-W mirror design).

4.3 Starting geometry

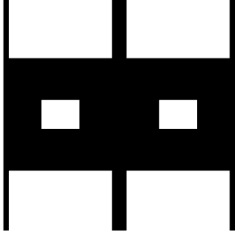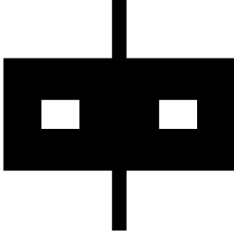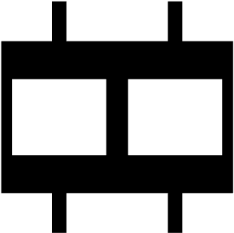**Table 3:** Starting Geometries and their designations
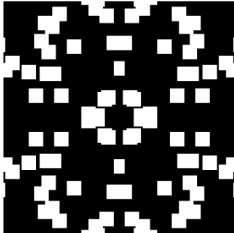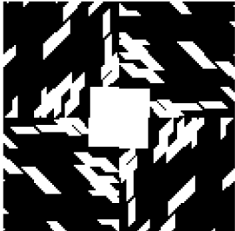
FP	**H**	**I**
Y	**Col1**	**Rand1**
Randss1	**Rsym1**	**Rsym2**

Table 3 shows the starting geometries used in this study. Multiple geometries can fulfill the same design requirement [13]. Investigating multiple seed geometries is an effort to explore the design space.

4.4 Alternate connectivity
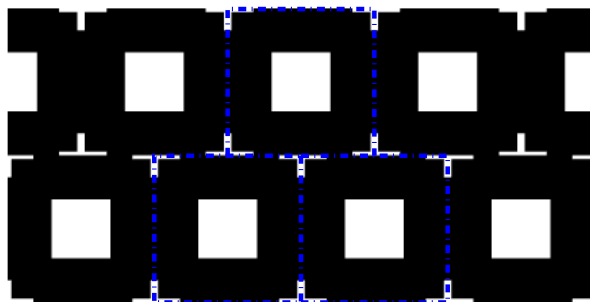
Figure 8: Depiction of alternate connnectivity of RUC's, halfwidth phase difference.

We also consider nonsimply connected RUC's in the structural model to open up the design space [22]. Notionally, this allowed the description of honeycomb structures in an intuitive or efficient manner. With reference to figure 8, it is best described as a brickwork connectivity (rather than corner-to-corner). In this study we only consider a halfwidth phase difference.

4.5 RVE size and windowing

$0 \text{ MPa} \leq \tau_{xy} \leq 10 \text{ MPa} \rightarrow$ grayscale
$10 \text{ MPa} < \tau_{xy} \leq 15 \text{ MPa} \rightarrow$ cyan.
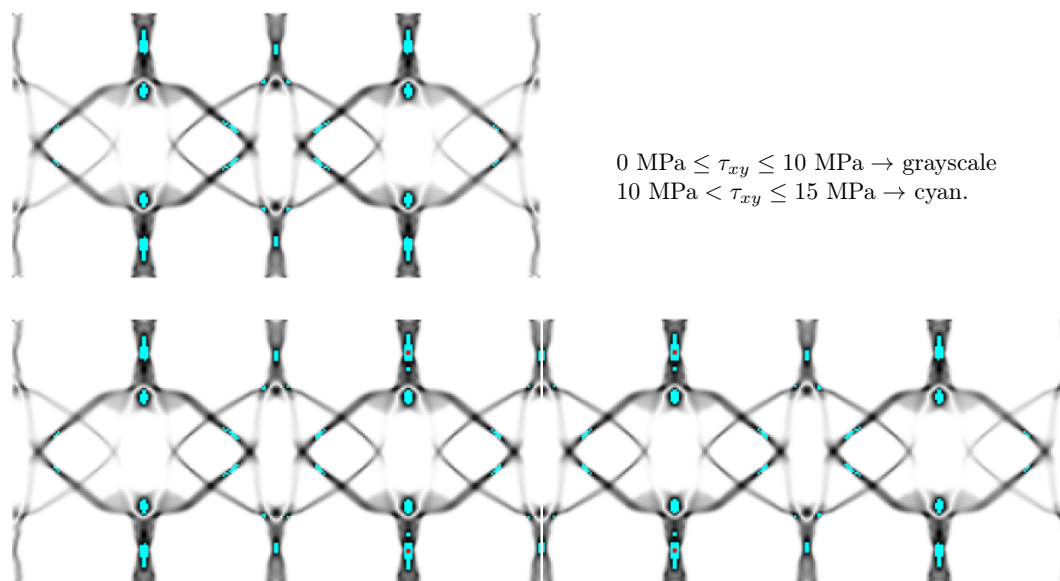
Figure 9: Shear stress distribution, RVE $2h$ wide (top), RVE $4h$ wide (bottom), same RUC geometry

An RVE $4h$ wide would be sufficient to describe a typical half-width of the contact patch. However, we apply a different methodology in order to reduce the considered RVE further, for sake of higher discretization in the RUC (RUC discretization of 128x128) to better explore the design space.

Figure 9 shows finite element analysis results of the same geometry - $2h$ vs $4h$. They are very similar in the central RUC's. In fact, only the end effects alter the average shear modulus. A

shear modulus calculated using the middle RUC's differs by 1% (vs 8% for entire domain). In an idea analogous to windowing in signal processing, we propose that the ends of the domain participate in the finite element calculation, but the average shear modulus is calculated only from the central RUC's. We calculate the sensitivities and functions using only central RUC's, but allow densities in the omitted regions to follow their central cousins.

We select $0.5h$ per side for the excluded section and use an overall domain size of $2h$ wide. Tests were performed with domains of $4h$. Results optimized in the windowed domains of $2h$ differed by 1% when analyzed in $4h$ wide domains. The maximum stress is also considered only in the windowed domain. For the adjoint implementation, we do not further partition according to the windowed and outside domains. Non-zero adjoint terms emerge from the outside elements. The outside elements are excluded from the $\frac{\partial}{\partial \rho_i}$ terms in the sensitivity calculations (and in the calculations of the functions themselves).
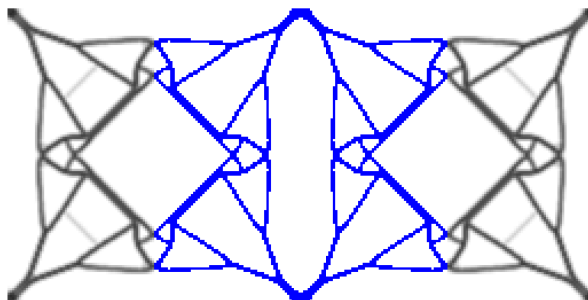

Figure 10: Example topology. Within window region in blue, outside region in grayscale.

5   Materials

In the main, we seek to use a base material for the NPT metamaterial that has a low intrinsic damping loss coefficient. A comparison of different material classes for various properties can be seen in the charts of Ashby [3]. In considering the instrinsic damping loss coefficient vs. Young's Modulus chart, elastomers have the required modulus for this application, however, they also have a high loss coefficient. This manifests as hysteretic heating. The "ideal" low modulus, low loss, monolithic material does not exist, necessitating material design via topology optimization. One selects a base material from the lower loss classes e.g. polymers and metals, considering a stochastic argument, that a lower starting (monolithic) modulus will provide a starting point that is closer to the ideal material, and will therefore increase the likelihood of a successful topology optimization.

Ju and Summers [20] investigated auxetic and regular honeycomb-based metamaterials for the NPT. Their candidate base materials were an aluminium alloy, titanium alloy and high strength steel. The basis of the initial selection was high yield strain. They used Cellular Material Theory [17] and considered plastic collapse of the structure. Reference [1] considered steel, aluminum alloy and polycarbonate in their topology optimization. They were able to generate an auxetic, re-entrant honeycomb in polycarbonate, however, generally struggled to achieve the design requirements in aluminium and steel. Given polycarbonate's elastic modulus of 2.7 GPa versus 70 GPa for Al; 210 GPa for steel, we take it that the topology optimization scheme found designs more easily within the higher volume fraction space of polycarbonate rather than aluminium or steel.

This study includes stress constraints, hence must include material properties related to stress.

Given the cyclic nature of the loading, fatigue strength is the most appropriate for the stress limit. The fatigue properties of steels are well established and often superior to other engineering alloys, however, given their intrinsic high modulus, we exclude this option. The fatigue properties of aluminium alloys are also well known from their use in the aerospace industry for structural components. The 10^6 endurance limit for 7075-T6 is 138 MPa [54]. We include magnesium alloy in this study. These have many automotive and aerospace applications where complex shapes and low mass are required. They typically have a Young's Modulus of 45 GPa, hence are a notional improvement on aluminium. Their fatigue properties can be good (depending on forming method and alloying). Values as high as 200 MPa can be achieved for 10^6 cycles [55]. Further, magnesium alloys can be formed into complex shapes via processes analogous to injection molding plastics [56]. This is useful if the NPT shear layer metamaterial has a complex topology.

The fatigue properties of unreinforced polycarbonate are relatively low (10 to 20 MPa for 10^6 cycles [57]). We substitute this with the semicrystalline thermoplastic, Polyetheretherketone (PEEK). It has a fatigue strength for 10^6 cycles of 50 to 80 MPa [57]. The penalty on Young's Modulus for PEEK is not high - 4 GPa (versus the 2.7 GPa of polycarbonate). We generally lower the above stated stress limits for the optimization to be conservative.

Table 4: Material properties used

Material	E [GPa]	ν [-]	σ_{lim} [MPa]
Aluminium alloy	70	0.33	100
Magnesium alloy	45	0.35	100
PEEK	4	0.4	40

6 Results

Table 5: Colour scale for Normalized Von Mises stress plots

Range	Colour
0 to 0.5	grayscale
0.5 to 0.75	cyan
0.75 to 1	blue
>1	red

The colour scheme listed in table 5 is used to plot the normalized Von Mises stress ($\frac{\sigma_{VM}}{\sigma_{lim}}$). For the depiction of the topology, the filtered density distribution is shown. The first optimization statement, equation 7, (and continuation on multiple limits) is designated *Cont.* While the second optimization statement, equation 8, with composite objective function and continuation only on stress limit, is designated *SigTorq*. For these results, the buckling constraint (equation 14) is excluded.

6.1 Stress results: metals

Optimization runs in Al alloy and Mg alloy were infeasible for the stress constraint. Though the stress limit is exceeded, this implies a fatigue life issue, not necessarily immediate rupture (within limits of applicability of linear model). We do not consider these materials further. Two examples are presented in figure 11 and figure 12.
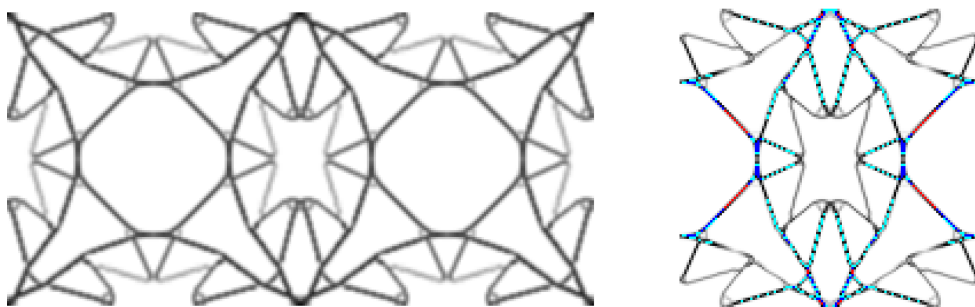

Figure 11: Stress-constrained optimized topology with continuation on volume, compliance and stress limits (*Cont*), on left. Normalized σ_{VM} distribution on right. Mg, Randss1 seed geometry, $45°$ symmetry, $V = 0.12$, $\sigma_{VM,max} = 120$ MPa
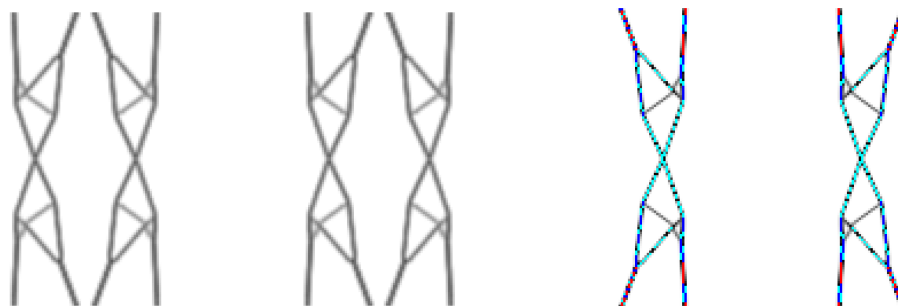
Figure 12: Stress-constrained optimized topology with continuation on stress limits (pseudo-Langrangian cost function, *SigTorq*) on the left. Normalized σ_{VM} distribution on the right. Mg, Col1 seed geometry, $V = 0.05$, $\sigma_{VM,max} = 117$ MPa

6.2 Stress results: PEEK

We shift our attention to topology optimization using the material, PEEK. Figure 13 and figure 14 that follow, show the topology of stress-constrained designs using the two different optimization statements (*Cont* and *SigTorq*), both starting with the Col1 geometry of Table 3.

Figure 13: Stress-constrained optimized topology with continuation on volume, compliance and stress limits (*Cont*), on left. Normalized σ_{VM} distribution on right. PEEK, Col1 seed geometry, $V = 0.13$, $\sigma_{VM,max} = 32$ MPa

Figure 14: Stress-constrained optimized topology with continuation on stress limits (pseudo-Langrangian cost function, *SigTorq*) on the left. Normalized σ_{VM} distribution on the right. PEEK, Col1 seed geometry, $V = 0.147$, $\sigma_{VM,max} = 32$ MPa

Figure 15 and figure 16, show the topology resulting from stress-constrained optimization using the two different optimization statements (*Cont* and *SigTorq*), both starting with the Randss1 geometry of Table 3.
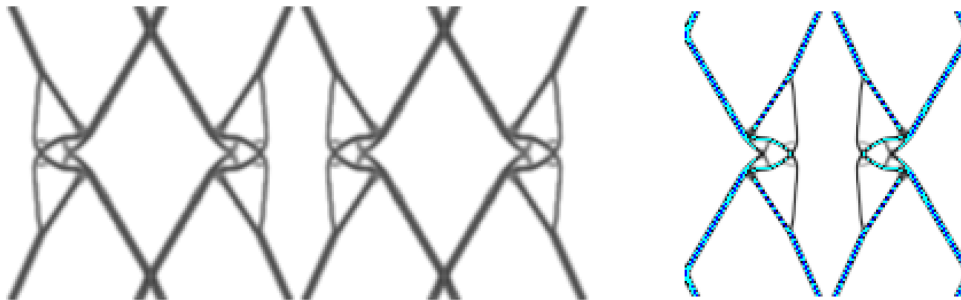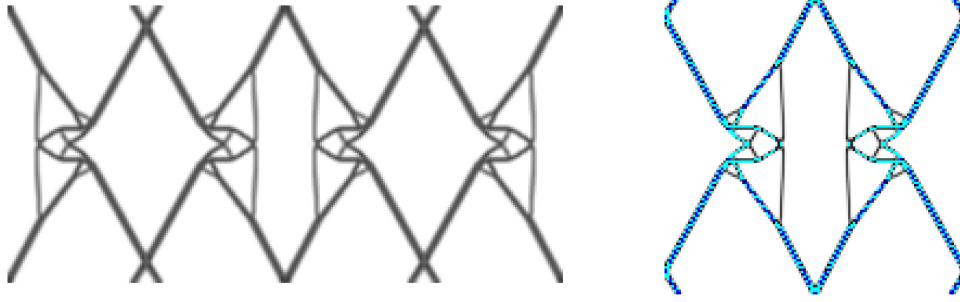

Figure 15: Stress-constrained optimized topology with continuation on volume, compliance and stress limits (*Cont*), on left. Normalized σ_{VM} distribution on right. PEEK, Randss1 seed geometry, $V = 0.10$, $\sigma_{VM,max} = 35$ MPa

Figure 16: Stress-constrained optimized topology with continuation on stress limits (pseudo-Langrangian cost function, *SigTorq*) on the left. Normalized σ_{VM} distribution on the right. PEEK, Randss1 seed geometry, $V = 0.094$, $\sigma_{VM,max} = 36$ MPa

Figure 17 and figure 18 show the topology of stress-constrained designs using the two different optimization statements (*Cont* and *SigTorq*), both starting with the Randss1 geometry of Table 3. The 45° symmetry is added.
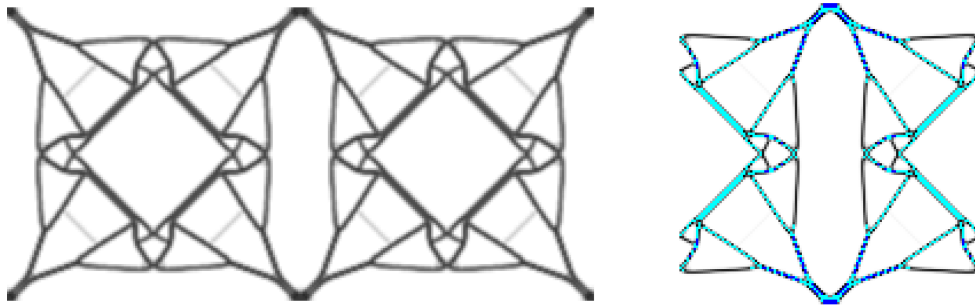

Figure 17: Stress-constrained optimized topology with continuation on volume, compliance and stress limits (*Cont*), on left. Normalized σ_{VM} distribution on right. PEEK, Randss1 seed geometry, 45° symmetry, $V = 0.12$, $\sigma_{VM,max} = 37$ MPa
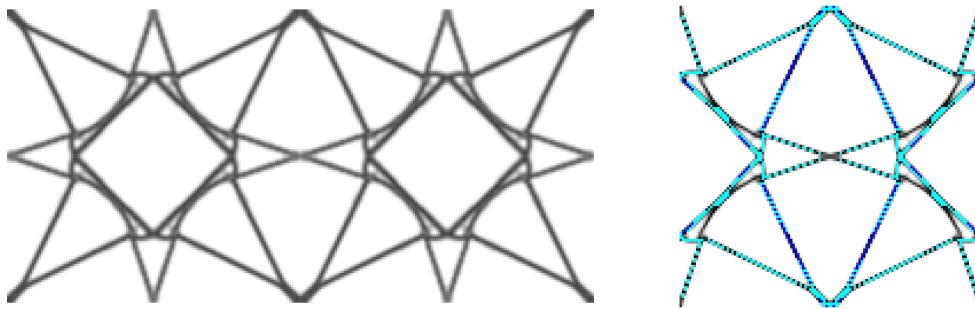

Figure 18: Stress-constrained optimized topology with continuation on stress limits (pseudo-Langrangian cost function, *SigTorq*) on the left. Normalized σ_{VM} distribution on the right. PEEK, Randss1 seed geometry, 45° symmetry, $V = 0.112$, $\sigma_{VM,max} = 37$ MPa

Figure 19 and figure 20 show the topology of stress-constrained designs using the two different optimization statements (*Cont* and *SigTorq*), both starting with the Rsym11 geometry of Table
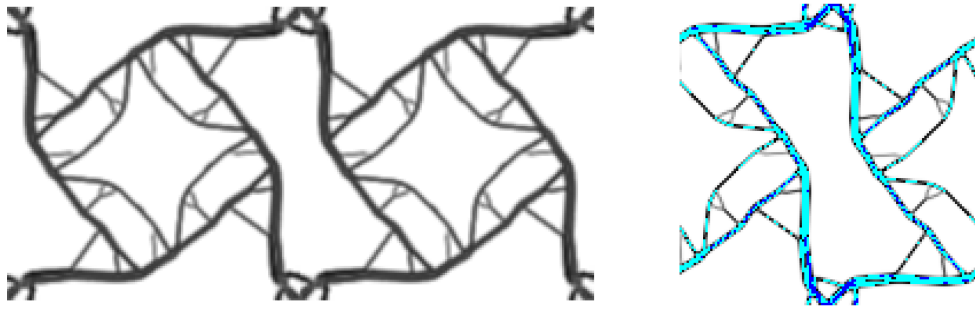
3. Rotational symmetry is added.

Figure 19: Stress-constrained optimized topology with continuation on volume, compliance and stress limits (*Cont*), on left. Normalized σ_{VM} distribution on right. PEEK, Rsym1 seed geometry, rotational symmetry, $V = 0.15$, $\sigma_{VM,max} = 39$ MPa
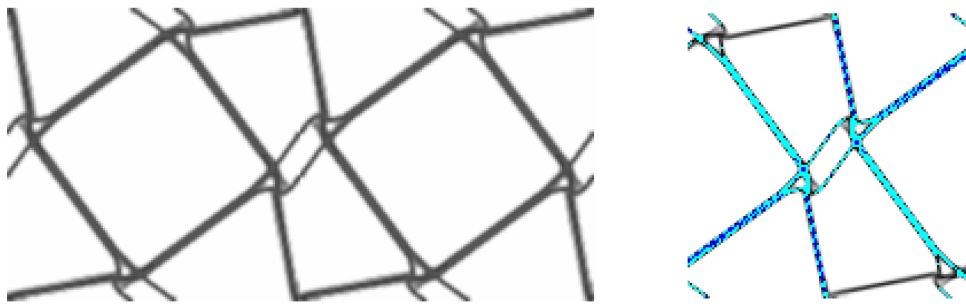

Figure 20: Stress-constrained optimized topology with continuation on stress limits (pseudo-Langrangian cost function, *SigTorq*) on the left. Normalized σ_{VM} distribution on the right. PEEK, Rsym1 seed geometry, rotational symmetry, $V = 0.105$, $\sigma_{VM,max} = 37$ MPa

Figure 21 and figure 22 depict the topology of stress-constrained optimizations both using the *SigTorq* optimization statement. The starting structures were the FP and Rand1 geometries of Table 3.
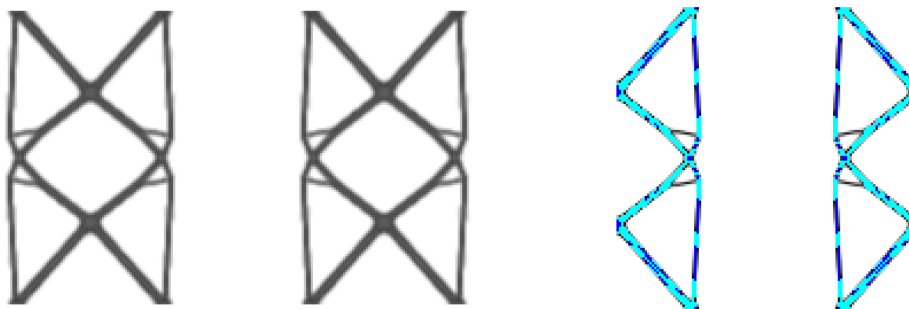

Figure 21: Stress-constrained optimized topology with continuation on stress limits (pseudo-Langrangian cost function, *SigTorq*) on the left. Normalized σ_{VM} distribution on the right. PEEK, FP seed geometry, $V = 0.096$, $\sigma_{VM,max} = 35$ MPa
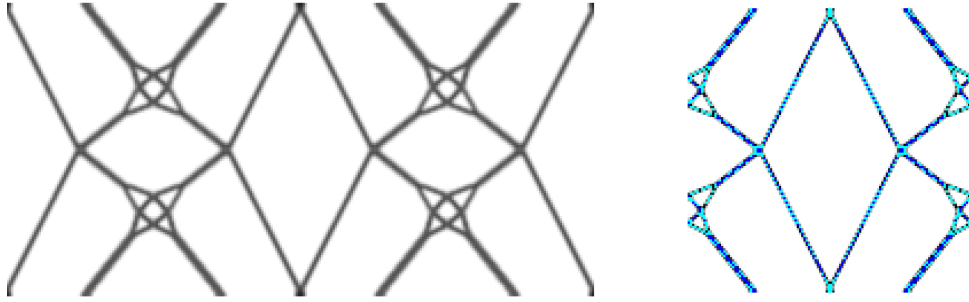
Figure 22: Stress-constrained optimized topology with continuation on stress limits (pseudo-Langrangian cost function, *SigTorq*) on the left. Normalized σ_{VM} distribution on the right. PEEK, Rand1 seed geometry, $V = 0.079$, $\sigma_{VM,max} = 37$ MPa

Figure 23 and figure 24 depict the topologies created by use of the *SigTorq* optimization statement. The stress constraint was negated i.e. the optimization only seeks to achieve the $\overline{G}$ requirement.
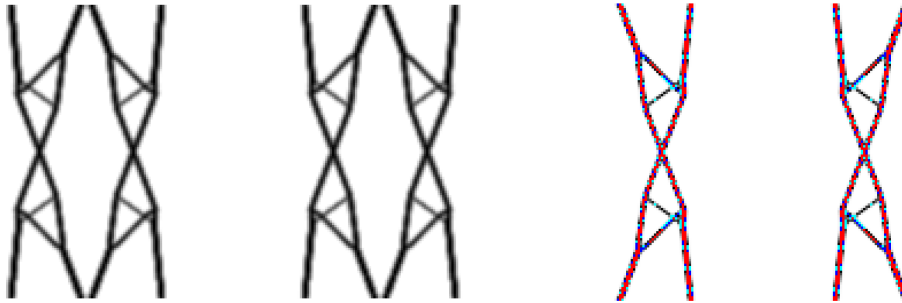

Figure 23: Optimized topology without stress limits (pseudo-Langrangian cost function, *SigTorq*) on the left. Normalized σ_{VM} distribution on the right. PEEK, Col1 seed geometry, $V = 0.102$, $\sigma_{VM,max} = 90$ MPa

Figure 24: Optimized topology without stress limits (pseudo-Langrangian cost function, *SigTorq*) on the left. Normalized σ_{VM} distribution on the right. PEEK, Randss1 seed geometry, $V = 0.068$, $\sigma_{VM,max} = 61$ MPa
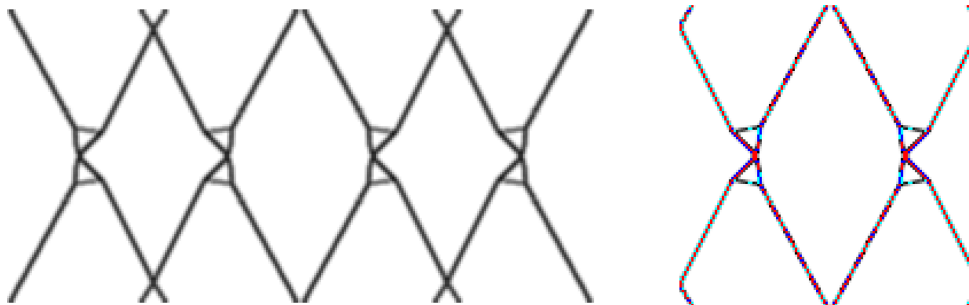
Figures 13 to 22 show optimized topologies that achieve the requirement of $\overline{G} = 10$ MPa while being within the stress constraint. The results indicate that the metamaterial design problem is

25

multi-modal or non-convex - multiple geometries can achieve the same target structural properties [13, 45]. Volume fractions were in the range 8 % to 15 %. This is similar to results in polycarbonate [1]. The low volume fraction is to be expected given the design objective to create a low effective shear modulus material from one that is three orders of magnitude higher as a monolith. The topologies are similar in performance with respect to stress. The majority of the volume is in the normalized stress range 0.5 to 0.75. Figures 13 to 16 are perhaps noteworthy for not having significant regions in the 0.75 to 1 range.

The two optimization statements and associated algorithms occasionally give similar topologies (e.g. compare figure 13 to figure 14 or figure 15 to figure 16). However, they are also capable of generating different topologies from the same starting geometry - see figure 17 versus figure 18 or figure 19 versus figure 20. Note, not all seed geometries shown in table 3 yielded converged, feasible solutions. Figure 15 has a diamond-like appearance, however, it is interesting to note that the diamond tip (intersection between RUC's) behaves like a compliant joint. The designs shown in figures 13, 14 and 21 comprise a family of similar topologies for this problem statement. Given that a low volume fraction is integral to the solution, a way of achieving this is with periodic empty spaces i.e. a columnar structure without connectivity between the RUC's. There is a minor analogy to the meso-structures investigated (as sizing problems) in Shankar et al. [7]. Figure 23 and figure 24 illustrate the effect of not having the stress constraint. The effective shear modulus is achieved with lower volume fraction designs than those obtained with the stress constraint.

6.3 Buckling results

We now focus on topology optimizations in PEEK, considering both stress and buckling constraints.

6.3.1 Buckling results $P_{lim} = 1$

Figure 25: Stress and buckling constrained optimized topology with continuation on volume, compliance and stress limits (*Cont*), on left. Normalized σ_{VM} distribution on right. PEEK, Randss1 seed geometry, $45°$ symmetry, $V = 0.132$, $\sigma_{VM,max} = 35$ MPa, $P_{lim} = 1$, $\frac{1}{P_1} = 0.85$.

Figure 26: Stress and buckling constrained optimized topology with continuation on stress limits (pseudo-Langrangian cost function, *SigTorq*) on the left. Normalized σ_{VM} distribution on the right. PEEK, Randss1 seed geometry, $45°$ symmetry, $V = 0.133$, $\sigma_{VM,max} = 38$ MPa, $P_{lim} = 1$, $\frac{1}{P_1} = 0.85$.
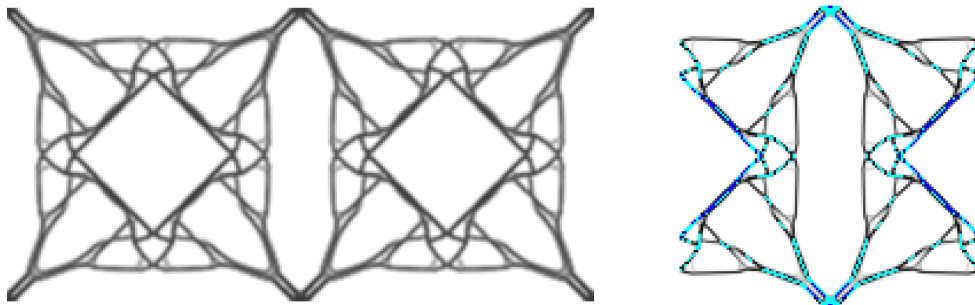

Figure 27: Stress and buckling constrained optimized topology with continuation on volume, compliance and stress limits (*Cont*), on left. Normalized σ_{VM} distribution on right. PEEK, Rsym1 seed geometry, rotational symmetry, $V = 0.15$, $\sigma_{VM,max} = 39$ MPa, $P_{lim} = 1$, $\frac{1}{P_1} = 0.90$.
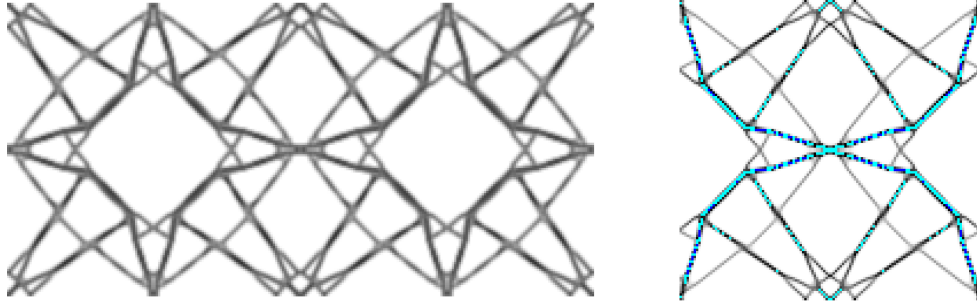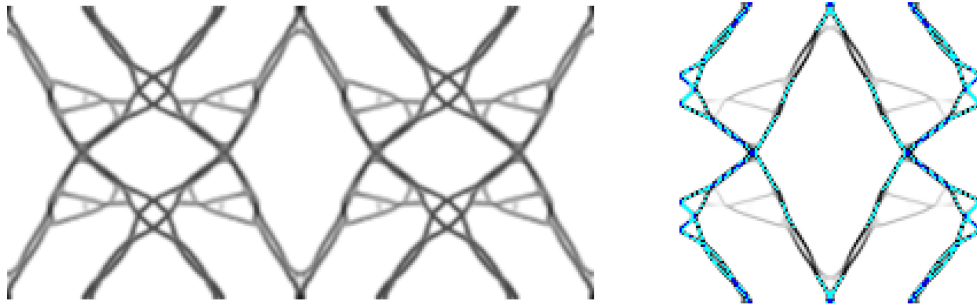

Figure 28: Stress and buckling constrained optimized topology with continuation on stress limits (pseudo-Langrangian cost function, *SigTorq*) on the left. Normalized σ_{VM} distribution on the right. PEEK, Rand1 seed geometry, $V = 0.105$, $\sigma_{VM,max} = 39$ MPa, $P_{lim} = 1$, $\frac{1}{P_1} = 0.83$.
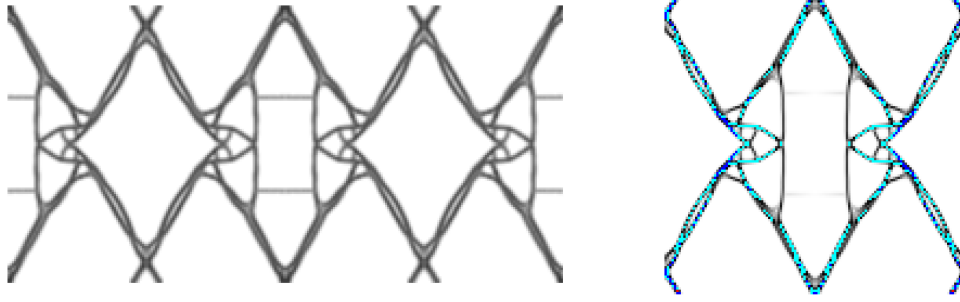
Figure 29: Stress and buckling constrained optimized topology with continuation on stress limits (pseudo-Langrangian cost function, *SigTorq*) on the left. Normalized σ_{VM} distribution on the right. PEEK, Randss1 seed geometry, $V = 0.109$, $\sigma_{VM,max} = 40$ MPa, $P_{lim} = 1$, $\frac{1}{P_1} = 0.90$.
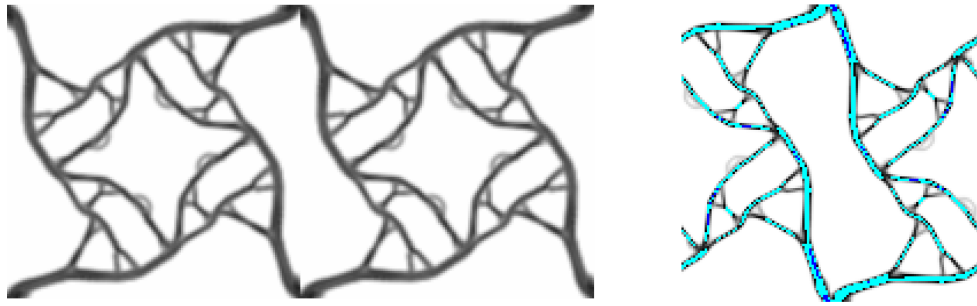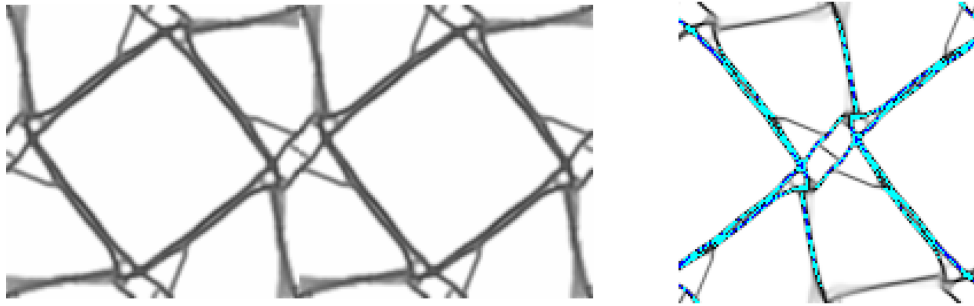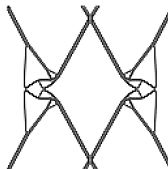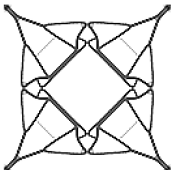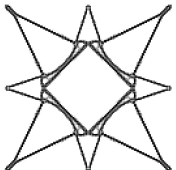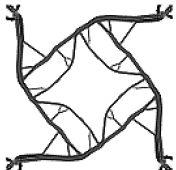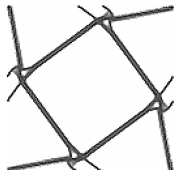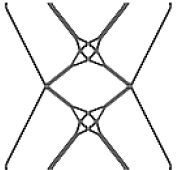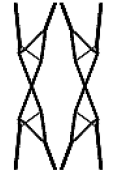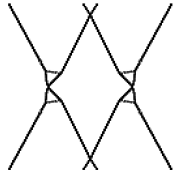

Figure 30: Stress and buckling constrained optimized topology with continuation on stress limits (pseudo-Langrangian cost function, *SigTorq*) on the left. Normalized σ_{VM} distribution on the right. PEEK, Rsym1 seed geometry, rotational symmetry, $V = 0.12$, $\sigma_{VM,max} = 38$ MPa, $P_{lim} = 1$, $\frac{1}{P_1} = 0.96$.
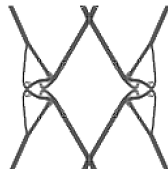
6.3.2 Buckling properties of stress constraint only designs

Table 6: Eigenvalues of designs optimized with stress constraint only

$\frac{1}{P_1} = 0.92$	$\frac{1}{P_1} = 0.39$	$\frac{1}{P_1} = 3.34$	$\frac{1}{P_1} = 3.40$
$\frac{1}{P_1} = 3.93$	$\frac{1}{P_1} = 6.13$	$\frac{1}{P_1} = 1.62$	$\frac{1}{P_1} = 2.91$
$\frac{1}{P_1} = 3.66$	$\frac{1}{P_1} = 1.27$	$\frac{1}{P_1} = 2.14$	$\frac{1}{P_1} = 10.02$

The buckling performance of the stress-only designs from section 6.2 are checked by calculating their eigenvalues. These are presented in table 6.

6.3.3 Buckling results: Discussion

Figures 25 to figure 30 achieve the required effective shear modulus, within the stress and buckling constraints. Noting the (generally) high eigenvalues of the stress-only designs in table 6, these topologies are susceptible to buckling failure. It is worth re-iterating the concern from Neves et al. [45], that the properties of extremal metamaterials are only valid for small loads, owing to possibility of buckling at higher loads. For a one-to-one comparison of the topologies achieved with the buckling and stress constraints, with those of the stress-only designs (same starting geometry) - see figure 25 versus figure 17, or figure 29 versus figure 16. There exists a visual similarity, however, the buckling-based designs tend to have a preponderance of finer structures. This was also observed in the results of Ferrari and Sigmund [49] and Gao and Ma [47], where monolithic structures tended to split, but remained interlinked by finer structures. However, they compared a compliance minimizing (stiffness maximizing) design to designs with the buckling constraint.

Slender structures initially would seem to be out of place in a buckling-based design. These designs usually have a higher volume fraction when compared to their stress-only counterparts. Higher volume fractions are associated with higher stiffness, however, each of these designs

(stress-only or buckling) achieve the same stiffness performance (equal effective shear modulus). (This is consistent with the results of Ferrari and Sigmund [49], but here constant stiffness is achieved with increased volume fraction.) Distributing the excess material in an area in the form of more slender members rather than a single monolithic member, allows for the optimized design to achieve the same shear modulus with a higher volume fraction. The more slender members experience lower average stresses than the thicker members along certain susceptible load paths. This improves the buckling performance (as a perturbation of the stress-only design). This truss-like arrangement (main members with thinner support members) is considered more resistant to global buckling modes [49]. Two of the columnar stress-only designs naturally have this topology (see table 6) and hence both could pass a $P_{lim} = 1$ buckling requirement. This is a further advantage of this family of designs (columnar, non-interconnected RUC's).

Metal foams were considered as candidate materials for the NPT shear layer, however, this has not been extensively investigated [5]. Without necessarily precluding such topologies, they could be susceptible to local buckling modes. An investigation would require a review of modelling strategy - length scale, descretization, RVE and homogenization. The more slender structures from the buckling designs also provide a research direction. It is plausible that a two-scale material - struts with a foam can further optimize the buckling design.

In general, the designs do suffer from some grayness, despite the SIMP implementation. This was something noted in Czech [26]. Numerical experimentation to higher SIMP exponents did not substantially alter this effect. One can interpret the grayness of the two-dimensional structure as an indicator of thickness in the third dimension.

7 Conclusions

The metamaterial for the shear band of an NPT is fertile ground for topology optimization, given the aim to lower the hysteretic loss by use of a base material with low intrinsic damping loss coefficient (material behaviour essentially elastic). To extend the body of knowledge, we have implemented stress and buckling constraints. We have also considered the impact of various starting geometries and symmetries. The base materials in the study are similar to those used in past studies, with minor modification due to an additional criterion requiring improved fatigue properties, along with a low elastic modulus. We consider the canonical case of $\overline{\gamma} = 10\%$ and $\overline{G} = 10$ MPa. This corresponds to a shear layer thickness of 7 mm.

Table 7: Base material properties vs. volume fraction of designs

Material	E [GPa]	V range [-]
Magnesium alloy	45	0.005 to 0.12
PEEK	4	0.08 to 0.15

The designs achieved are typically of low volume fraction, with an inverse relationship to the base material elastic modulus - see table 7. With semicrystalline thermoplastic, PEEK, having the lowest elastic modulus, it gave the highest volume fraction designs. Metals have an elastic modulus at least an order higher than plastics, hence they have fewer feasible designs for the optimization algorithm to seek. Consequently it was easier to explore the design space with PEEK. While material removal (volume constraint or volume minimization) was fundamental to the optimization routines, having sufficient material to work with, is a lower bound that ensures a variety of topologies. PEEK is also a good candidate material for additive manufacturing. The two opti-

mization routines used, in combination with the various symmetries and starting geometries, led to unique topologies that fulfilled the effective shear modulus and stress constraint. Generally though, these designs do have poor buckling performance. The linear buckling constraint tended to push the the designs toward finer, more complex topologies - splitting larger structures into more slender combinations. While this appears counterintuitive, it is understandable, due to the increased volume fraction and alteration of stresses in susceptible load paths (when compared with stress-only designs). A particular family of designs (columnar, non-interconnected RUC's) that emerged in this study, appears to exhibit favourable properties for this application.

Appendices

A Adjoint formulation

The residual vector, $\boldsymbol{R}$, partitioned according to free (f) and prescribed (p) degrees of freedom is given by:

$$\begin{bmatrix} \boldsymbol{R^p} \\ \boldsymbol{R^f} \end{bmatrix} = \begin{bmatrix} \boldsymbol{K^{pp}} & \boldsymbol{K^{pf}} \\ \boldsymbol{K^{fp}} & \boldsymbol{K^{ff}} \end{bmatrix} \begin{bmatrix} \boldsymbol{u^p} \\ \boldsymbol{u^f} \end{bmatrix} - \begin{bmatrix} \boldsymbol{F^p} \\ \boldsymbol{F^f} \end{bmatrix} = \boldsymbol{0}, \tag{20}$$

where the $\boldsymbol{K^{ij}}$ are the partitioned blocks of the global stiffness matrix. Following the derivation in James and Waisman [32], we define:

$$\Pi = f + \begin{bmatrix} \boldsymbol{\psi^{pT}} & \boldsymbol{\psi^{fT}} \end{bmatrix} \begin{bmatrix} \boldsymbol{R^p} \\ \boldsymbol{R^f} \end{bmatrix}, \tag{21}$$

noting that we can select the adjoint terms, $\boldsymbol{\psi}$, such that the implicit derivatives of the unknown state variables, $\boldsymbol{y} = \begin{bmatrix} \boldsymbol{F^p} \\ \boldsymbol{u^f} \end{bmatrix}$, vanish. The variable f represents an arbitrary function of interest, which can be the objective or a constraint function. Note that the implicit derivatives of the unknown state variables are computationally costly to evaluate. Therefore, eliminating these terms via the adjoint formulation reduces the total computational cost of the sensitivity analysis. We take the total derivative of equation 21 with respect to the design variables, x_i and apply the chain rule:

$$\frac{d\Pi}{dx_i} = \frac{df}{dx_i} = \frac{\partial f}{\partial x_i} + \begin{bmatrix} \frac{\partial f}{\partial \boldsymbol{F^p}} & \frac{\partial f}{\partial \boldsymbol{u^f}} \end{bmatrix} \begin{bmatrix} \frac{d\boldsymbol{F^p}}{dx_i} \\ \frac{d\boldsymbol{u^f}}{dx_i} \end{bmatrix}$$
$$+ \boldsymbol{\psi^{pT}} \left(\frac{\partial \boldsymbol{R^p}}{\partial x_i} + \begin{bmatrix} \frac{\partial \boldsymbol{R^p}}{\partial \boldsymbol{F^p}} & \frac{\partial \boldsymbol{R^p}}{\partial \boldsymbol{u^f}} \end{bmatrix} \begin{bmatrix} \frac{d\boldsymbol{F^p}}{dx_i} \\ \frac{d\boldsymbol{u^f}}{dx_i} \end{bmatrix} \right) + \boldsymbol{\psi^{fT}} \left(\frac{\partial \boldsymbol{R^f}}{\partial x_i} + \begin{bmatrix} \frac{\partial \boldsymbol{R^f}}{\partial \boldsymbol{F^p}} & \frac{\partial \boldsymbol{R^f}}{\partial \boldsymbol{u^f}} \end{bmatrix} \begin{bmatrix} \frac{d\boldsymbol{F^p}}{dx_i} \\ \frac{d\boldsymbol{u^f}}{dx_i} \end{bmatrix} \right). \tag{22}$$

Thereafter we group terms containing the implicit derivatives of the state variables. By setting each sum of these terms to zero, the implicit derivatives vanish. These equations then yield the solution for the adjoint vector:

$$\begin{aligned} \frac{d\boldsymbol{F^p}}{dx_i} \left(\frac{\partial f}{\partial \boldsymbol{F^p}} + \boldsymbol{\psi^{pT}} \frac{\partial \boldsymbol{R^p}}{\partial \boldsymbol{F^p}} + \boldsymbol{\psi^{fT}} \frac{\partial \boldsymbol{R^f}}{\partial \boldsymbol{F^p}} \right) &= \boldsymbol{0}, \\ \frac{d\boldsymbol{u^f}}{dx_i} \left(\frac{\partial f}{\partial \boldsymbol{u^f}} + \boldsymbol{\psi^{pT}} \frac{\partial \boldsymbol{R^p}}{\partial \boldsymbol{u^f}} + \boldsymbol{\psi^{fT}} \frac{\partial \boldsymbol{R^f}}{\partial \boldsymbol{u^f}} \right) &= \boldsymbol{0}. \end{aligned} \tag{23}$$

In the general case, equation 23, defines the adjoint terms as a coupled linear system:

$$\begin{bmatrix} \frac{\partial \mathbf{R^p}}{\partial \mathbf{F^p}}^T & \frac{\partial \mathbf{R^f}}{\partial \mathbf{F^p}}^T \\ \frac{\partial \mathbf{R^p}}{\partial \mathbf{u^f}}^T & \frac{\partial \mathbf{R^f}}{\partial \mathbf{u^f}}^T \end{bmatrix} \begin{bmatrix} \boldsymbol{\psi^p} \\ \boldsymbol{\psi^f} \end{bmatrix} = \begin{bmatrix} -\frac{\partial f}{\partial \mathbf{F^p}}^T \\ -\frac{\partial f}{\partial \mathbf{u^f}}^T \end{bmatrix}, \tag{24}$$

though typically, zero terms (as will be seen) allows for simplification of equation 24 in determining the adjoint solution. Collecting the remaining non-zero terms, equation 22 reduces to the following, which gives an expression for the total sensitivity of f with respect to the design parameter x_i:

$$\frac{d\Pi}{dx_i} = \frac{df}{dx_i} = \frac{\partial f}{\partial x_i} + \boldsymbol{\psi^p}^T \frac{\partial \mathbf{R^p}}{\partial x_i} + \boldsymbol{\psi^f}^T \frac{\partial \mathbf{R^f}}{\partial x_i} = \frac{\partial f}{\partial x_i} + \boldsymbol{\psi}^T \frac{\partial \mathbf{R}}{\partial x_i}, \tag{25}$$

where $\boldsymbol{\psi} = \begin{bmatrix} \boldsymbol{\psi^p} \\ \boldsymbol{\psi^f} \end{bmatrix}$.

B Objective function sensitivity

Refer to a fundamental text like Zienkiewicz et al. [58] for standard linear elastic FEM implementation and definitions. Assume stress, $\boldsymbol{\sigma}$, and strain, $\boldsymbol{\epsilon}$, are defined in matrix form, 2-D. Given $\boldsymbol{\epsilon_e} = \boldsymbol{B}\boldsymbol{u_e}$ and $\boldsymbol{\sigma_e} = \boldsymbol{E}\boldsymbol{\epsilon_e}$ (where $\boldsymbol{B}$ is the traditional strain displacement matrix), the (Gauss) average shear stress, $\overline{\tau}_{e,i}$, and shear strain, $\overline{\gamma}_{e,i}$, within element i are:

$$\begin{aligned} \overline{\tau}_{e,i} &= \frac{1}{A_{e,i}} G_0 \rho_{e,i}{}^p \left(\sum_{gauss} |J| \boldsymbol{B}_{row3} \right) \cdot \boldsymbol{u_{e,i}}, \\ \overline{\gamma}_{e,i} &= \frac{1}{A_{e,i}} \left(\sum_{gauss} |J| \boldsymbol{B}_{row3} \right) \cdot \boldsymbol{u_{e,i}}, \end{aligned} \tag{26}$$

where $\sum\limits_{gauss}$ indicates numerical integration by gauss qaudrature, $|J|$ is the Jacobian determinant required for element mapping, G_0 is the base material shear modulus, $A_{e,i}$ is the element area and $\boldsymbol{u_{e,i}}$ is the element displacements. Hence the objective function in FE form is:

$$\overline{G} = \frac{\sum\limits_{i=1}^{N_e} \overline{\tau}_{e,i}}{\sum\limits_{i=1}^{N_e} \overline{\gamma}_{e,i}}. \tag{27}$$

Note here that N_e is the number of elements in the RVE (i.e. entire domain) and that the average strain is included for completeness. Due to the chosen loading, the average strain is prescribed. Hence the above is modified with fixed input strain, $\overline{\gamma}_{inp}$, as:

$$\overline{G} = \frac{\sum\limits_{i=1}^{N_e} \overline{\tau}_{e,i}}{N_e \overline{\gamma}_{inp}}. \tag{28}$$

Applying the adjoint equations and definitions to the objective function, $\overline{G}$ gives:

$$\begin{aligned} \boldsymbol{\psi^p} &= \mathbf{0}, \\ \boldsymbol{K^{ff}}\boldsymbol{\psi^f} &= -\frac{\partial f}{\partial \boldsymbol{u^f}}^T. \end{aligned} \tag{29}$$
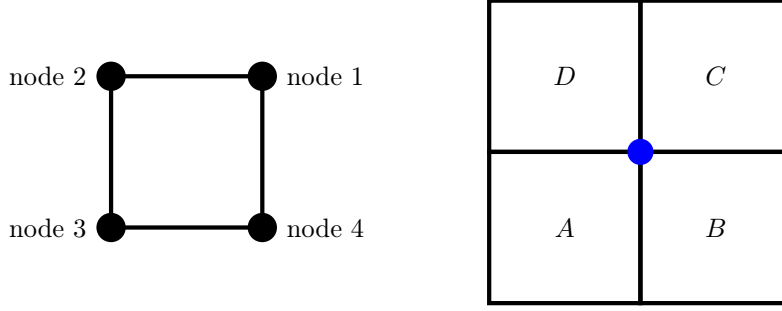
Figure 31: Node numbering and typical element connectivity for 4-node quad (for understanding sensitivity calculation). Elements labelled A to D

Noting that a given node (displacement) is associated with (at most) 4 elements (in this scheme, though this can be generalized), 4 elements then contribute to each $\frac{\partial f}{\partial u_i}$ term - see figure 31. Defining the following: $\beta_{kl} = \frac{1}{A_{e,i}} \sum_{gauss} B_{kl}|J|$, the gradient is then:

$$
\begin{array}{rcl}
\frac{\partial \overline{G}}{\partial u_{ix}} & = & \frac{G_0}{N_e \overline{\gamma}_{inp}} (\rho_A{}^p \beta_{31} + \rho_B{}^p \beta_{33} + \rho_C{}^p \beta_{35} + \rho_D{}^p \beta_{37}), \\
\frac{\partial \overline{G}}{\partial u_{iy}} & = & \frac{G_0}{N_e \overline{\gamma}_{inp}} (\rho_A{}^p \beta_{32} + \rho_B{}^p \beta_{34} + \rho_C{}^p \beta_{36} + \rho_D{}^p \beta_{38}).
\end{array}
\tag{30}
$$

We write the local element stiffness as: $\boldsymbol{k_e} = \rho^p \boldsymbol{k_{e0}}$. The variable, N_{RUC}, is the number of representative unit cells in the RVE (hence instances of elements with shared densities) and $N_{e,RUC}$ is number of elements in RUC. We define an $N_{e,RUC} \times N_{RUC}$ matrix s, where s_{ij} is the global index of the element (one of N_{RUC}) associated with a given ρ_i.

The implicit term of the total adjoint sensitivity expression, $\boldsymbol{\psi}^T \frac{\partial \boldsymbol{R}}{\partial x_i}$, may be computed element-wise as:

$$
\boldsymbol{\psi}^T \frac{\partial \boldsymbol{R}}{\partial \rho_i} = \sum_{j=1}^{N_{RUC}} \boldsymbol{\psi}_{e,s_{ij}}{}^T p \rho_i{}^{p-1} \boldsymbol{k_{e0}} \boldsymbol{u}_{e,s_{ij}},
\tag{31}
$$

The explicit term is then also computed element-wise using:

$$
\frac{\partial \overline{G}}{\partial \rho_i} = \frac{G_0}{N_e \overline{\gamma}_{inp}} \sum_{j=1}^{N_{RUC}} p \rho_i{}^{p-1} \boldsymbol{\beta}_{row3} \cdot \boldsymbol{u}_{e,s_{ij}}.
\tag{32}
$$

C   Stress function sensitivity

Given the 2-D Von Mises stress definition is:

$$
\sigma_{VM}{}^2 = \sigma_x{}^2 + \sigma_y{}^2 + \sigma_x \sigma_y + 3 \tau_{xy}{}^2,
\tag{33}
$$

we define matrix, $\boldsymbol{M}$ as:

$$
\boldsymbol{M} = \begin{bmatrix} 1 & -\frac{1}{2} & 0 \\ -\frac{1}{2} & 1 & 0 \\ 0 & 0 & 3 \end{bmatrix}.
\tag{34}
$$

This allows for the FE definition of element average Von Mises stress as:

$$
\overline{\sigma}_{VM,i}{}^2 = \frac{1}{A_{e,i}} \boldsymbol{u}_{e,i}{}^T \left(\sum_{gauss} |J| \boldsymbol{B}^T \boldsymbol{E} \boldsymbol{M} \boldsymbol{E} \boldsymbol{B} \right) \boldsymbol{u}_{e,i}.
\tag{35}
$$

Grouping terms that are constant for a uniform mesh, linear, small strain analysis and applying the SIMP formulation, define matrix, $\boldsymbol{k_{VM0}}$,:

$$
\begin{aligned}
\boldsymbol{k_{VM0}} &= \tfrac{1}{A_{e,i}} \left(\sum_{gauss} |J| \boldsymbol{B^T E_0 M E_0 B} \right), \\
\overline{\sigma}_{VM,i} &= \rho_{e,i}{}^p \left(\boldsymbol{u}_{e,i}{}^T \boldsymbol{k_{VM0}} \boldsymbol{u}_{e,i} \right)^{\frac{1}{2}}.
\end{aligned}
\tag{36}
$$

We further define, the following function of element displacements, for brevity:

$$
\Delta_{e,i} \left(\boldsymbol{u}_{e,i} \right) = \boldsymbol{u}_{e,i}{}^T \boldsymbol{k_{VM0}} \boldsymbol{u}_{e,i}.
\tag{37}
$$

The FE form of the stress constraint is given by:

$$
g_{nl2} = \left[\sum_{i=1}^{N_e} \left(\rho_i{}^{\eta+p} \frac{\Delta_{e,i}{}^{\frac{1}{2}}}{\sigma_{lim}} \right)^q \right]^{\frac{1}{q}} - (1 + \epsilon) \leq 0.
\tag{38}
$$

Applying the adjoint equations yields the same as equation 29 ($\frac{\partial g_{nl2}}{\partial \boldsymbol{u^f}}$ being different). Letting:

$$
\Upsilon = \left[\sum_{i=1}^{N_e} \left(\rho_i{}^{\eta+p} \frac{\Delta_{e,i}{}^{\frac{1}{2}}}{\sigma_{lim}} \right)^q \right],
\tag{39}
$$

the following is required to calculate the adjoint term (using notation related to figure 31 and equation 30):

$$
\frac{\partial g_{nl2}}{\partial u_j} = \Upsilon^{\frac{1-q}{q}} \sum_{i=A}^{D} \left(\frac{\rho_i{}^{\eta+p}}{\sigma_{lim}} \right)^q \Delta_{e,i}{}^{\frac{q}{2}-1} \boldsymbol{k_{VM0,rowk}} \cdot \boldsymbol{u}_{e,i}.
\tag{40}
$$

That is, 4 elements affect the sensitivity with respect to a given DOF. This is used in an equation similar to equation 31. Here k is the position in the element displacement that is associated with u_j. The partial or *explicit* sensitivity term for density is:

$$
\frac{\partial g_{nl2}}{\partial \rho_i} = (\eta + p) \, \rho_i{}^{[(\eta+p)q-1]} \Upsilon^{\frac{1-q}{q}} \sum_{j=1}^{N_{RUC}} \left(\frac{\Delta_{s_{ij}}{}^{\frac{1}{2}}}{\sigma_{lim}} \right)^q.
\tag{41}
$$

D   Buckling function sensitivity

Kim [59] gives a definition of the geometric stiffness matrix, $\boldsymbol{k_G}$, as:

$$
\boldsymbol{k_G} = \int_{\Omega} \boldsymbol{B_G^T \Xi B_G} d\Omega,
\tag{42}
$$

where for 2-D, 4 node elements:

$$
\boldsymbol{\Xi} = \begin{bmatrix} \sigma_x & \tau_{xy} & 0 & 0 \\ \tau_{xy} & \sigma_y & 0 & 0 \\ 0 & 0 & \sigma_x & \tau_{xy} \\ 0 & 0 & \tau_{xy} & \sigma_y \end{bmatrix},
\tag{43}
$$

$$
\boldsymbol{B_G} = \begin{bmatrix} \frac{\partial N_1}{\partial x} & 0 & \frac{\partial N_2}{\partial x} & 0 & \frac{\partial N_3}{\partial x} & 0 & \frac{\partial N_4}{\partial x} & 0 \\ \frac{\partial N_1}{\partial y} & 0 & \frac{\partial N_2}{\partial y} & 0 & \frac{\partial N_3}{\partial y} & 0 & \frac{\partial N_4}{\partial y} & 0 \\ 0 & \frac{\partial N_1}{\partial x} & 0 & \frac{\partial N_2}{\partial x} & 0 & \frac{\partial N_3}{\partial x} & 0 & \frac{\partial N_4}{\partial x} \\ 0 & \frac{\partial N_1}{\partial y} & 0 & \frac{\partial N_2}{\partial y} & 0 & \frac{\partial N_3}{\partial y} & 0 & \frac{\partial N_4}{\partial y} \end{bmatrix},
\tag{44}
$$

and N_i is the shape function of node i.

We seek to write $\boldsymbol{\Xi_{e,i}}$ in FE form with its displacement dependency made explicit. Recalling the Gauss integrated matrix β from Appendix B, we define:

$$\begin{aligned}
\boldsymbol{\Gamma} &= \boldsymbol{E\beta}, \\
\boldsymbol{\Gamma_0} &= \boldsymbol{E_0\beta},
\end{aligned} \tag{45}$$

where $\boldsymbol{\Gamma}$ is 3×8. Hence:

$$\boldsymbol{\Xi_{e,i}} = \begin{bmatrix} \boldsymbol{\Gamma}_{row1} & \boldsymbol{\Gamma}_{row3} & 0 & 0 \\ \boldsymbol{\Gamma}_{row3} & \boldsymbol{\Gamma}_{row2} & 0 & 0 \\ 0 & 0 & \boldsymbol{\Gamma}_{row1} & \boldsymbol{\Gamma}_{row3} \\ 0 & 0 & \boldsymbol{\Gamma}_{row3} & \boldsymbol{\Gamma}_{row2} \end{bmatrix} \begin{bmatrix} \boldsymbol{u}_{e,i} & 0 & 0 & 0 \\ 0 & \boldsymbol{u}_{e,i} & 0 & 0 \\ 0 & 0 & \boldsymbol{u}_{e,i} & 0 \\ 0 & 0 & 0 & \boldsymbol{u}_{e,i} \end{bmatrix}. \tag{46}$$

Eventually the elemental stress stiffness matrix may be written as:

$$\boldsymbol{k}_{G,e,i} = \overbrace{\begin{bmatrix} \boldsymbol{\kappa_{11}} & 0 & \boldsymbol{\kappa_{12}} & 0 & \boldsymbol{\kappa_{13}} & 0 & \boldsymbol{\kappa_{14}} & 0 \\ 0 & \boldsymbol{\kappa_{11}} & 0 & \boldsymbol{\kappa_{12}} & 0 & \boldsymbol{\kappa_{13}} & 0 & \boldsymbol{\kappa_{14}} \\ \boldsymbol{\kappa_{21}} & 0 & \dots & \dots & \dots & \dots & \boldsymbol{\kappa_{24}} & 0 \\ 0 & \boldsymbol{\kappa_{21}} & \dots & \dots & \dots & \dots & 0 & \boldsymbol{\kappa_{24}} \\ \vdots & \vdots & \vdots & \vdots & \vdots & \vdots & \vdots & \vdots \\ \boldsymbol{\kappa_{41}} & 0 & \dots & \dots & \dots & \dots & \boldsymbol{\kappa_{44}} & 0 \\ 0 & \boldsymbol{\kappa_{41}} & \dots & \dots & \dots & \dots & 0 & \boldsymbol{\kappa_{44}} \end{bmatrix}}^{\boldsymbol{\kappa\kappa}_{Ge}} \underbrace{\overbrace{\begin{bmatrix} \boldsymbol{u}_{e,i} & 0 & 0 & \dots & \dots & \dots & \dots & 0 \\ 0 & \boldsymbol{u}_{e,i} & 0 & \dots & \dots & \dots & \dots & 0 \\ 0 & 0 & \searrow & \dots & \dots & \dots & \dots & 0 \\ \vdots & \vdots & \vdots & \ddots & \vdots & \vdots & \vdots & \vdots \\ 0 & 0 & 0 & 0 & 0 & 0 & 0 & \boldsymbol{u}_{e,i} \end{bmatrix}}^{\boldsymbol{k}_{uGe}}}_{64 \times 8},$$

$$\underbrace{}_{8 \times 64}$$

$$\tag{47}$$

where

$$\underbrace{\boldsymbol{\kappa_{mn}}}_{1 \times 8} = \frac{\partial N_m}{\partial x}\frac{\partial N_n}{\partial x}\boldsymbol{\Gamma}_{row1} + \left(\frac{\partial N_m}{\partial x}\frac{\partial N_n}{\partial y} + \frac{\partial N_m}{\partial y}\frac{\partial N_n}{\partial x}\right)\boldsymbol{\Gamma}_{row3} + \frac{\partial N_m}{\partial y}\frac{\partial N_y}{\partial x}\boldsymbol{\Gamma}_{row2}. \tag{48}$$

The second matrix in equation 47, has further notation related to its differentiation with respect to displacement:

$$
\boldsymbol{dk_{uGe,n}} = \xrightarrow[\text{in } 8\times 1]{\text{position } n}
\begin{bmatrix}
\begin{bmatrix} \vdots \\ 0 \\ 1 \\ 0 \\ \vdots \end{bmatrix} & \vdots & \vdots & & & & & \vdots \\
0 & 0 & 0 & & & & & 0 \\
1 & 0 & 0 & \dots & \dots & \dots & \dots & 0 \\
0 & 0 & 0 & & & & & 0 \\
\vdots & \vdots & \vdots & & & & & \vdots \\
\vdots & \begin{bmatrix} \vdots \\ 0 \\ 1 \\ 0 \\ \vdots \end{bmatrix} & \vdots & & & & & \vdots \\
0 & 0 & 0 & & & & & 0 \\
0 & 1 & 0 & \dots & \dots & \dots & \dots & 0 \\
0 & 0 & 0 & & & & & 0 \\
\vdots & \vdots & \vdots & & & & & \vdots \\
\mathbf{0} & \mathbf{0} & \searrow & \dots & \dots & \dots & \dots & \mathbf{0} \\
\vdots & \vdots & \vdots & \ddots & \vdots & \vdots & \vdots & \vdots \\
\vdots & & & & & \vdots & & \begin{bmatrix} \vdots \\ 0 \\ 1 \\ 0 \\ \vdots \end{bmatrix} \\
0 & & & & & 0 & & 0 \\
0 & \dots & \dots & \dots & \dots & \dots & 0 & 1 \\
0 & & & & & 0 & & 0 \\
\vdots & & & & & \vdots & & \vdots
\end{bmatrix}, \tag{49}
$$

and $n = 1, 2, ..., 8$. Applying adjoint equations to equation 14 yields the same as equation 29 ($\frac{\partial g_{nl3}}{\partial \boldsymbol{u^f}}$ being different). For brevity let:

$$
\begin{aligned}
\Upsilon_b &= \left[\sum_{j=1}^{N_{eig}} \left(\frac{\boldsymbol{\phi_j}^T \boldsymbol{K_G}^{\boldsymbol{ff}} \boldsymbol{\phi_j}}{\boldsymbol{\phi_j}^T \boldsymbol{K}^{\boldsymbol{ff}} \boldsymbol{\phi_j}} \right)^q \right], \\
\Theta_{K,j} &= \boldsymbol{\phi_j}^T \boldsymbol{K}^{\boldsymbol{ff}} \boldsymbol{\phi_j}, \\
\Theta_{G,j} &= \boldsymbol{\phi_j}^T \boldsymbol{K_G}^{\boldsymbol{ff}} \boldsymbol{\phi_j}.
\end{aligned} \tag{50}
$$

The following is required to calculate the adjoint term (using notation related to figure 31) :

$$
\frac{\partial g_{nl3}}{\partial u_m} = P_{lim} \Upsilon_b^{\frac{1-q}{q}} \sum_{j=1}^{N_{eig}} \left(\frac{\Theta_{G,j}{}^{q-1}}{\Theta_{K,j}{}^q} \right) \sum_{i=A}^{D} \left(\boldsymbol{\phi_{e,j}}^T \boldsymbol{\kappa \kappa_{Ge}} \boldsymbol{dk_{uGe,i}} \boldsymbol{\phi_{e,j}} \right). \tag{51}
$$

Note that the eigenvector terms are expressed in an element-wise fashion. The explicit derivative with respect to density is:

$$
\begin{aligned}
\frac{\partial g_{nl3}}{\partial \rho_i} =&P_{lim} \Upsilon_b^{\frac{1-q}{q}} \sum_{m=1}^{N_{RUC}} \sum_{j=1}^{N_{eig}} \left(\frac{1}{P_j} \right)^{q-1} \frac{1}{\Theta_{K,j}{}^2} \\
&\left((p+1)\rho_i{}^p \Theta_{K,j} \left(\boldsymbol{\phi_{e,j}}^T \boldsymbol{\kappa \kappa_{Ge0}} \boldsymbol{k_{uGe,s_{im}}} \boldsymbol{\phi_{e,j}} \right) + p\rho_i{}^{p-1} \Theta_{G,j} \left(\boldsymbol{\phi_{e,j}}^T \boldsymbol{k_{e,0}} \boldsymbol{\phi_{e,j}} \right) \right),
\end{aligned} \tag{52}
$$

recalling our alternate penalization for the stress stiffness versus the conventional stiffness matrix.

References

[1] C. Czech, N. Thyagaraja, G. M. Fadel, and P. Guarneri. Systematic design optimization of the metamaterial shear beam of a nonpneumatic wheel for low rolling resistance. *Journal of Mechanical Design*, 137:041404–1–9, 2015.

[2] T. B. Rhyne and S. M. Cron. Development of a non-pneumatic wheel. *Tire Science & Technology*, 34(3):150–169, 2006.

[3] M. F. Ashby. *Materials Selection in Mechanical Design*. Butterworth-Heinemann, Oxford, United Kingdom, 4th edition, 2011.

[4] N. Thyagaraja, P. Shankar, G. M. Fadel, and P. Guarneri. Optimizing the shear beam of a non-pneumatic wheel for low rolling resistance. In *Proceedings of the ASME 2011 International Design Engineering Technical Conferences & Computers and Information in Engineering Conference*. ASME, 2011. DETC2011-48532.

[5] M. Fazelpour and J. D. Summers. Evolution of meso-structures for non-pneumatic tire development: A case study. In *Proceedings of the ASME 2014 International Design Engineering Technical Conferences & Computers and Information in Engineering Conference*. ASME, 2014. DETC2014-34184.

[6] L. A. Berglind, J. Ju, and J. D. Summers. Aluminum taper bristle-shaped shear band for a non-pneumatic tire. *Tire Science & Technology*, 40(3):152–170, 2012.

[7] P. Shankar, M. Fazelpour, and J. D. Summers. Comparative study of optimization techniques in sizing mesostructures for use in nonpneumatic tires. *Journal of Computing and Information Science in Engineering*, 15:041009–1–6, 2015.

[8] M. P. Bendsøe and N. Kikuchi. Generating optimal topologies in structural design using a homogenization method. *Computer Methods in Applied Mechanics and Engineering*, 71: 197–224, 1988.

[9] H. A. Eschenauer and N. Olhoff. Topology optimization of continuum structures: A review. *Applied Mechanics Reviews*, 54(4):331–390, 2001.

[10] M. P. Bendsøe and O. Sigmund. *Topology Optimization: Theory, Methods and Applications*. Springer-Verlag, Berlin, Germany, 2nd edition, 2004.

[11] O. Sigmund. Tailoring materials with prescribed elastic properties. *Mechanics of Materials*, 20:351–368, 1995.

[12] O. Sigmund. A new class of extremal composites. *Journal of the Mechanics and Physics of Solids*, 48:397–428, 2000.

[13] L. Xia and P. Breitkopf. Design of materials using topology optimization and energy-based homogenization approach in Matlab. *Structural & Multidisciplinary Optimization*, 52:1229–1241, 2015.

[14] S. Amstutz, S. M. Giusti, A. A. Novotny, and E. A. de Souza Neto. Topological derivative for multi-scale linear elasticity models applied to the synthesis of microstructures. *International Journal for Numerical Methods in Engineering*, 84:733–756, 2010.

[15] O. Sigmund and S Torquato. Design of materials with extreme thermal expansion using a three-phase topology optimization method. *Journal of the Mechanics and Physics of Solids*, 45(6):1037–1067, 1997.

[16] L. Gibiansky and O. Sigmund. Multiphase composites with extremal bulk modulus. *Journal of the Mechanics and Physics of Solids*, 48:461–498, 2000.

[17] L. J. Gibson, M. F. Ashby, G. S. Schajer, and C. I. Robertson. The mechanics of two-dimensional cellular materials. *Proceedings of the Royal Society A*, 382:25–42, 1982.

[18] P. Shankar, J. Ju, J. D. Summers, and J. C. Ziegert. Design of sinusoidal auxetic structures for high shear flexure. In *Proceedings of the ASME 2010 International Design Engineering Technical Conferences & Computers and Information in Engineering Conference*. ASME, 2010. DETC2010-28545.

[19] A. Kolla, J. Ju, J. D. Summers, G. Fadel, and J. C. Ziegert. Design of chiral honeycomb meso-structures for high shear flexure. In *Proceedings of the ASME 2010 International Design Engineering Technical Conferences & Computers and Information in Engineering Conference*. ASME, 2010. DETC2010-28557.

[20] J. Ju and J. D. Summers. Compliant hexagonal periodic lattice structures having both high shear strength and high shear strain. *Materials & Design*, 32(2):512–524, 2011.

[21] P. Shankar, M. Fazelpour, and J. D Summers. An energy-based approach for design of meso-structures with high shear flexure. In *Proceedings of the ASME 2013 International Design Engineering Technical Conferences and Computers and Information in Engineering Conference*. ASME, 2013. DETC2013-12292.

[22] C. Czech, P. Guarneri, J. Gibert, and G. Fadel. On the accurate analysis of linear elastic meta-material properties for use in design optimization problems. *Composites Science and Technology*, 72(5):580–586, 2012.

[23] A. Drago and M.-J. Pindera. Micro-macromechanical analysis of heterogeneous materials: Macroscopically homogeneous vs periodic microstructures. *Composites Science and Technology*, 67:1243–1263, 2007.

[24] B. Hassani and E. Hinton. A review of homogenization and topology optimization I - homogenization theory for media with periodic structure. *Computers and Structures*, 69: 707–717, 1998.

[25] C. Czech, P. Guarneri, and G. Fadel. Using non-simply connected unit cells in the multiscale analysis and design of meta-materials. In *12th AIAA Aviation Technology, Integration, and Operations (ATIO) Conference*. AIAA, 2012. 2012-5445.

[26] C. Czech. *Design of Meta-Materials Outside the Homogenization Limit Using Multiscale Analysis and Topology Optimization*. PhD thesis, Clemson University, Clemson, SC, 2012.

[27] M. P. Bendsøe. Optimal shape design as a material distribution problem. *Structural Optimization*, 1:193–202, 1989.

[28] M. P. Bendsøe and O. Sigmund. Material interpolation schemes in topology optimization. *Archive of Applied Mechanics*, 69:635–654, 1999.

[29] K. A. James, J. S. Hansen, and J. R. R. A. Martins. Structural topology optimization for multiple load cases using a dynamic aggregation technique. *Engineering Optimization*, 41 (12):1103–1118, 2009.

[30] E. Lee, K. A. James, and J. R. R. A. Martins. Stress-constrained topology optimization with design-dependent loading. *Structural and Multidisciplinary Optimization*, 46:647–661, 2012.

[31] J. Sobieszczanski-Sobieski. Sensitivity of complex, internally coupled systems. *AIAA Journal*, 28(1):153–160, 1990.

[32] K. A. James and H. Waisman. Failure mitigation in optimal topology design using a coupled nonlinear continuum damage model. *Computer Methods in Applied Mechanics and Engineering*, 268:614–631, 2014.

[33] O. Sigmund and J. Petersson. Numerical instabilities in topology optimization:a survey on procedures dealing with checkerboards, mesh-dependencies and local minima. *Structural Optimization*, 16:68–75, 1998.

[34] O. Sigmund. On the design of compliant mechanisms using topology optimization. *Mechanics of Structures and Machines*, 25(4):493–524, 1997.

[35] T. Bruns and D. Tortorelli. Topology optimization of non-linear elastic structures and compliant mechanisms. *Computer Methods in Applied Mechanics and Engineering*, 190: 3443–3459, 2001.

[36] G. D. Cheng and X. Guo. ϵ-relaxed approach in stuctural topology optimization. *Structural Optimization*, 13:258–266, 1997.

[37] P. Duysinx and M. P. Bendsøe. Topology optimization of continuum structures with local stress constraints. *International Journal for Numerical Methods in Engineering*, 43:1453–1478, 1988.

[38] K. A. James, E. Lee, and J. R. R. A. Martins. Stress-based topology optimization using an isoparametric level set method. *Finite Elements in Analysis and Design*, 58:20–30, 2012.

[39] R. J. Yang and C. J. Chen. Stress-based topology optimization. *Structural Optimization*, 12:98–105, 1996.

[40] J. Paris, F. Navarrina, I. Colominas, and M. Casteleiro. Block aggregation of stress constraints in topology optimization of structures. *Advances in Engineering Software*, 41:433–441, 2010.

[41] J. Le, C. Norato, T. Bruns, C. Ha, and D. Tortorelli. Stress-based topology optimization for continua. *Structural and Multidisciplinary Optimization*, 41:605–620, 2010.

[42] M. M. Neves, H. Rodrigues, and M. Guedes. Generalized topology design of structures with a buckling load criterion. *Structural Optimization*, 11:71–78, 1995.

[43] H. Rodrigues, M. Guedes, and M. P. Bendsøe. Necessary conditions for optimal design of structures with a nonsmooth eigenvalue based criterion. *Structural Optimization*, 9:52–56, 1995.

[44] F. H. Clarke. *Optimization and Non-Smooth Analysis*. John Wiley & Sons, New York, 1983.

[45] M. M. Neves, O. Sigmund, and M. P. Bendsøe. Topology optimization of periodic microstructures with a penalization of highly localized buckling modes. *International Journal for Numerical Methods in Engineering*, 54:809–834, 2002.

[46] N. L. Pedersen. Maximization of eigenvalues using topology optimization. *Structural & Multidisciplinary Optimization*, 20:2–11, 2000.

[47] X. Gao and X. Ma. Topology optimization of continuum structures under buckling constraints. *Computers and Structures*, 157:142–152, 2015.

[48] T. H. H. Pian and K. Sumihara. Rational approach for assumed stress finite elements. *International Journal for Numerical Methods in Engineering*, 20:1685–1695, 1984.

[49] F. Ferrari and O. Sigmund. Revisiting topology optimization with buckling constraints. *Structural & Multidisciplinary Optimization*, 2019. doi: `https://doi.org/10.1007/s00158-019-02253-3`.

[50] K. Svanberg. The method of moving asymptotes - a new method for structural optimization. *International Journal for Numerical Methods in Engineering*, 24:359–373, 1987.

[51] K. Svanberg. A class of globally convergent optimization methods based on conservative convex separable approximations. *SIAM Journal on Optimization*, 12(2):555–573, 2002.

[52] O. Sigmund. Design of multiphysics actuators using topology optimization - Part I: One-material structures. *Computer Methods in Applied Mechanics and Engineering*, 190:6577–6604, 2001.

[53] G. I. N. Rozvany. A critical review of established methods of structural topology optimization. *Structural & Multidisciplinary Optimization*, 37:217–237, 2009.

[54] R. C. Juvinall and K. M. Marshek. *Fundamentals of Machine Component Design*. John-Wiley & Sons, New York, 2nd edition, 1991.

[55] J. F. King. Technology of magnesium and magnesium alloys. In H. E. Friedrich and B. L. Mordike, editors, *Magnesium Technology: Metallurgy, Design Data, Applications*, chapter 6, pages 219–430. Springer-Verlag, Berlin, Germany, 2006.

[56] G. Cole. Automotive Applications in North America. In H. E. Friedrich and B. L. Mordike, editors, *Magnesium Technology: Metallurgy, Design Data, Applications*, chapter 8.2, pages 569–603. Springer-Verlag, Berlin, Germany, 2006.

[57] L. W. McKeen. *Fatigue and Tribological Properties of Plastics and Elastomers*. William Andrew, Cambridge, Massachusetts, U.S.A., 3rd edition, 2016.

[58] O. C. Zienkiewicz, R. L. Taylor, and J. Z. Zhu. *The Finite Element Method: Its Basis and Fundamentals*. Butterworth-Heinemann, Oxford, United Kingdom, 7th edition, 2013.

[59] N. H. Kim. *Introduction to Nonlinear Finite Element Analysis*. Springer, New York, 2018.